Materials Advances

PAPER

Unveiling photocatalytic functionalities of (Gd³⁺, Mo⁶⁺) co-doped BiVO₄ nanoparticles: an experimental–DFT approach

Nusaibah Ehsan,[a] Md. Rafatul Haq,[a] Sadiq Shahriyar Nishat, [b]
Quazi Shafayat Hossain,[a] Shirin Akter Jahan,[c] M. N. I. Khan, [d]
Umme Sarmeen Akhtar,[c] Muhammad Shahriar Bashar,[e] H. N. Das, [d] Dipa Islam,[f]
Md. Zakir Sultan, [g] Sharmin Jahan,[h] Khandker Saadat Hossain[i] and
Imtiaz Ahmed [*a]

Efficient photocatalysts capable of toxic dye degradation using perennial solar radiation have tremendous potential in environmental remediation. Herein, a surfactant-free hydrothermal process was used to synthesize undoped bismuth vanadate $BiVO_4$ and (Gd³⁺, Mo⁶⁺) co-doped $Bi_{1-x}Gd_xV_{1-y}Mo_yO_4$ (x = 0.02, 0.04, 0.06, 0.08, 0.10; y = 0.02) nanoparticles. The presence of mixed monoclinic scheelite (ms) and tetragonal zircon (tz) phases in the as-synthesized nanoparticles due to co-doping was quantified from Rietveld refined X-ray diffraction, Raman, and Fourier transform infrared spectroscopy. Field emission scanning electron microscopy images revealed buck-horn and rod-shaped nanoparticles with an average size of 80–130 nm for undoped and co-doped samples, respectively. The good crystallinity of the (Gd³⁺, Mo⁶⁺) co-doped samples was corroborated by high-resolution transmission electron microscopy. The desired chemical oxidation states of all constituent elements of the co-doped samples were confirmed from X-ray photoelectron spectroscopy. The suitable valence band edge position for driving photocatalytic reactions was observed from ultraviolet photoelectron spectroscopy. The diffuse reflectance measurements implied an increase in the electronic band gap due to co-doping. Hubbard U corrected density functional theory (DFT+U) indicates a shallow trap center in the co-doped samples in favor of reduced electron–hole recombination, which was also supported by photoluminescence intensity reduction. The $Bi_{0.94}Gd_{0.06}V_{0.98}Mo_{0.02}O_4$ photocatalyst degraded 96% of the highly concentrated 50 ppm methylene blue dye over 180 min under simulated sunlight with a reaction rate of 0.01524 min⁻¹. This impressive photocatalytic efficiency can be ascribed to the synergistic effect of the mixed ms–tz phase, small nanoparticle size, good crystallinity, reduced carrier recombination, and proper band edge alignment of the $Bi_{0.94}Gd_{0.06}V_{0.98}Mo_{0.02}O_4$ photocatalyst.

[a] Materials Science Research Laboratory, Department of Electrical and Electronic Engineering, University of Dhaka, Dhaka-1000, Bangladesh.
E-mail: imtiaz@du.ac.bd

[b] Department of Materials Science and Engineering, Rensselaer Polytechnic Institute, Troy, New York 12180, USA

[c] Institute of Glass and Ceramic Research and Testing, Bangladesh Council of Scientific and Industrial Research, Dhaka-1205, Bangladesh

[d] Materials Science Division, Atomic Energy Centre, Dhaka-1000, Bangladesh

[e] Institute of Energy Research and Development, Bangladesh Council of Scientific and Industrial Research, Dhaka-1205, Bangladesh

[f] Biomedical and Toxicological Research Institute, Bangladesh Council of Scientific and Industrial Research, Dhaka-1205, Bangladesh

[g] Centre for Advanced Research in Sciences, University of Dhaka, Dhaka-1000, Bangladesh

[h] Institute of Food Science and Technology, Bangladesh Council of Scientific and Industrial Research, Dhaka-1205, Bangladesh

[i] Nanophysics and Soft Matter Laboratory, Department of Physics, University of Dhaka, Dhaka-1000, Bangladesh

1. Introduction

Photocatalytic degradation is perhaps the most effective, affordable, and eco-friendly way of eliminating colored organic dyes from waste for environmental cleanup.[1–4] To this end, the n-type semiconductor photocatalyst $BiVO_4$, with three distinctive monoclinic scheelite (ms), tetragonal scheelite (ts), and tetragonal zircon (tz) crystalline phases, has attracted considerable research interest owing to its capabilities of producing highly reactive radicals by harnessing solar energy, essential for eliminating toxic dyes.[5–9] Its promise stems from advantageous characteristics like benignity, stability, low-cost, appropriate band locations, narrow band gap ($\sim$2.4 eV in ms phase), and pronounced optical absorption.[10,11] Nevertheless, slow separation and a rapid recombination rate of photogenerated

electron–hole pairs (EHPs) put severe constraints on the photocatalytic activity of $BiVO_4$.[12–14] Several strategies have been explored, based on experimental and first principles density functional theory (DFT), to mitigate the shortcomings of $BiVO_4$, such as metal doping, facet control, heterojunction formation, semiconductor recombination, and incorporation of functional materials.[15–26] Of these approaches, chemical doping with metal ions has been demonstrated as an effective technique for modifying the crystalline phase along with distortion in the $[VO_4]^-$ and $[BiO_8]^-$ units, morphology, and electronic structure for enhancing the photocatalytic performance of $BiVO_4$.[27,28]

There are several reports on attempts to mitigate photogenerated carrier recombination in $BiVO_4$ by mono-doping rare-earth (RE) lanthanides (e.g., Ce, Eu, Gd) and transition metals (TMs) (e.g., Fe, Co, Ni) into the Bi-sites, leveraging their f and d orbitals. On the contrary, few reports on co-doping of the Bi-sites with RE elements exist. Noor et al. demonstrated photocatalytic dye degradation performance enhancement by Gd^{3+} and Y^{3+} co-dpoing into the Bi-site.[29] Obregón et al. reported superior photocatalytic degradation for Er^{3+} and Y^{3+} co-doping of the Bi-site of $BiVO_4$.[30] Jia et al. observed higher photocatalytic degradation for La^{3+} and Gd^{3+} co-doped $BiVO_4$.[31] Regmi et al. co-doped the Bi-site with an RE trio (Yb^{3+}, Er^{3+}, Tm^{3+}) to achieve notable photocatalytic degradation.[12] There are reports on (Fe^{3+}, Cu^{2+}), (Cu^{2+}, Zn^{2+}), and (Mn^{2+}, Zn^{2+}) co-doping into the Bi-site that enhanced the photocatalytic activity.[32–34]

In recent times, the use of two distinct elements selectively substituted for Bi^{3+} and V^{5+} ions in $BiVO_4$ has drawn considerable research interest, as it substantially affects the material's structural and phase properties. For instance, Ce^{3+}/Mo^{6+} co-doping created a mixed ms–tz phase, while Fe^{3+}/W^{6+} co-doping caused a transition to an orthorhombic structure.[35,36] In contrast, Zr^{4+}/W^{6+} co-doping maintained the desired ms phase of $BiVO_4$.[37] Now, Gd^{3+} (93.8 pm) can act as an isovalent dopant for Bi^{3+} (103 pm), and can reduce the hole effective mass, and enhance the carrier separation and photocatalytic performance.[38,39] The comparable ionic radii of Mo^{6+} (59 pm) and V^{5+} (54 pm) enable molybdenum to function as an n-type dopant on vanadium sites in $BiVO_4$, producing shallow impurity states that facilitate the separation of photo-induced electrons and holes, thereby improving the photocatalytic efficiency.[40–45] Can we leverage these favorable attributes of Gd^{3+}/Mo^{6+} dopants synergistically? To the best of our knowledge, the effect of Gd^{3+}/Mo^{6+} co-doping of Bi^{3+}/V^{5+} on the structural, morphological, electronic structure, and photocatalytic performance of $BiVO_4$ has rarely been reported.

Here, we synthesized undoped and (Gd^{3+}, Mo^{6+}) co-doped $BiVO_4$ nanoparticles with $Bi_{1-x}Gd_xV_{1-y}Mo_yO_4$ ($x = 0.02, 0.04, 0.06, 0.08, 0.10$; $y = 0.02$) stoichiometry via a surfactant-free hydrothermal process. Detailed structural and ms–tz phase explorations of all as-synthesized nanoparticles are presented using X-ray diffraction, Raman, and Fourier transform infrared spectroscopy. The surface morphology variation, crystallinity, and elemental identification of the nanoparticles were probed using scanning and transmission electron microscopy and energy dispersive X-ray spectroscopy, respectively. The desired

chemical oxidation states and valence band structure were analyzed using X-ray and ultraviolet photoelectron spectroscopy. The effects of co-doping on the electronic structure of BVO were quantified from combined diffuse reflectance measurements and DFT simulations. The photogenerated carrier recombination of the nanoparticles was captured from photoluminescence measurements. The superior methylene blue (50 ppm) dye degradation capabilities of co-doped $BiVO_4$ were corroborated from UV-vis absorption measurements and band edge alignment analysis. Overall, this work may have presented detailed information in favor of the superior photocatalytic performance of (Gd^{3+}, Mo^{6+}) co-doped $BiVO_4$ nanoparticles.

2. Methodology

2.1. Computational details

The Vienna Ab Initio Simulation Package VASP 6.3.1 code was used to model the core-valence interaction with the projector-augmented wave (PAW) method.[46–48] The PAW considered 15 electrons of $Bi-5d^{10}6s^26p^3$, 11 electrons of $V-3p^63d^44s^1$, 6 electrons of $O-2s^22p^4$, 18 electrons of $Gd-5s^25p^64f^75d^16s^2$, and 12 electrons of $Mo-4p^64d^55s^1$ in valence configurations, and treated the remaining ones as the core. For the undoped $BiVO_4$, a total of 198 atoms in a $2 \times 2 \times 2$ supercell having 32 Bi atoms, 32 V atoms, and 128 O atoms, were considered (see Fig. S1). To incorporate varying degrees of Gd concentration in the simulation, four different supercells with 1, 2, 3, and 4 Bi atoms replaced by Gd atoms were considered, to obtain 3.125, 6.25, 9.375, and 12.5% Gd concentration levels, respectively. To emulate 2% Mo doping in all co-doped structures, one V atom was replaced by a Mo atom in the supercell to achieve 3.125% Mo doping level. The structural relaxations were performed with self-consistent electronic and Hellmann–Feynman ionic convergences of 10^{-5} eV per atom and 10^{-2} eV Å^{-1}, respectively. The plane-wave energy cut-off was set to 500 eV. The $2 \times 2 \times 2$ Monkhorst–Pack (MP) k-mesh was used to perform Brillouin zone (BZ) integrations. A logical choice for the exchange correlation functional (XCF) based on a balance between computational complexities and precision is crucial in DFT simulations.[49,50] We made use of Hubbard interaction U corrected DFT+U to boost dilute Coulomb interaction of the localized V-3d and applied $U = 4.8, 3.1, 2$, and 2.3 eV in Bi-6p, V-3d, O-2p, and Mo-4d, respectively.[18,51–56] For the localized Gd-4f orbitals, $U = 6$ eV was used based on the findings of ref. 57 and 58.

2.2. Sample preparation

7.72 mmol (3.746 g) $Bi(NO_3)_3 \cdot 5H_2O$ (99.99%, Sigma) and 7.72 mmol (0.906 g) NH_4VO_3 (99%, Sigma) were dissolved in 15 ml of 2 M HNO_3 (as a transparent clear solution) and 70 mL of deionized (DI) water ($\sim$18 MΩ) heated to 65 °C (as a transparent yellow solution), respectively, under vigorous magnetic stirring (650 rpm) for 2 h. The NH_4VO_3 solution was added dropwise from a burette into $Bi(NO_3)_3 \cdot 5H_2O$ subjected to constant magnetic stirring. The solution turned into an

opaque, yellow-colored, dense suspension as 25 wt% NH_4OH was added to fix the pH = 9, and loaded into a 100 mL Teflon-lined autoclave for hydrothermal reaction at 180 °C for 48 h inside an oven. The sample was naturally cooled to room temperature, centrifuged (10 000 rpm), washed (6 consecutive cycles in DI water and ethanol alternately), and dried at 120 °C for 48 h. The dried powder was sintered at 400 °C for 2 h and subsequently ground in a mortar pestle for 1 h. The final bright yellow product is termed as u-BVO hereafter. In the case of the (Gd^{3+}, Mo^{6+}) co-doped samples $Bi_{1-x}Gd_xV_{1-y}Mo_yO_4$, the same hydrothermal technique was implemented where $Gd(NO_3)_3 \cdot 6H_2O$ (99+ %, Sigma) and $(NH_4)_2MoO_4$ (99+ %, Sigma) were dissolved into 15 mL of 2 M HNO_3 and 20 mL of DI water in stoichiometric proportions, respectively. The co-doped $Bi_{1-x}Gd_xV_{1-y}Mo_yO_4$ samples, where x is varied as 0.02, 0.04, 0.06, 0.08, and 0.10 while keeping the y fixed at 0.02, were subsequently termed as Gx%My%-BVO. The sintered co-doped samples appeared yellowish-white and turned to light yellow after grinding for 1 h.

2.2.1. Photocatalytic sample preparation. The methylene blue (MB) dye solutions were prepared at two different concentrations of 50 and 100 ppm in 100 mL of DI water. Both the undoped and co-doped photocatalyst concentrations were set to 1 g L^{-1}. The pH of the dye-catalyst mixture was set to 10 by adding the required amount of NH_4OH solution. The desired adsorption–desorption equilibrium in the mixture was established by 30 min of magnetic stirring in the dark state. The synthetic solar irradiation was provided from a 100 W Hg–Xe lamp with a fused silica exposure window. During the photocatalytic exposure, constant magnetic stirring prevented unwanted dye concentration gradients from occurring in the solution, thereby eliminating spurious degradation effects. Photocatalytic measurements were performed at an ambient temperature of $\sim$300 K. The photocatalyst removal was done with high-speed centrifugation and the UV-vis absorption of the dye solution was recorded at 30 min intervals over a 180 min measurement time.

2.3. Characterization techniques

The powdered X-ray diffraction (XRD) data of all as-synthesized samples were obtained within the 10° to 80° angular range (0.02° step, scan speed 2° min^{-1}) from a Rigaku SmartLab SE multipurpose XRD system operating at a tube voltage and current of 40 kV and 40 mA, respectively. The Raman modes (calibrated with a Si 520.7 cm^{-1} photon peak) were obtained in a Horiba Scientific LabRAM HR evolution confocal Raman microscope operating with a 532 nm green laser. The infrared absorption bands were captured by using a PerkinElmer spectrum Fourier transform infrared (FTIR) spectrometer. For surface morphology, elemental purity and spatial distribution analysis, a field emission scanning electron microscope (FESEM, JEOL 7610F) coupled with an energy dispersive X-ray (EDX) detector (Model: JED 2300) and a scanning electron microscope (SEM, AVO 18) with EDX (Model: EDAX Team) were used. The high resolution transmission electron microscope (HRTEM) and selected area electron diffraction (SAED) images were recorded with a Talos F200X TEM operating at 200 kV. The elemental binding energy measurements were performed by an
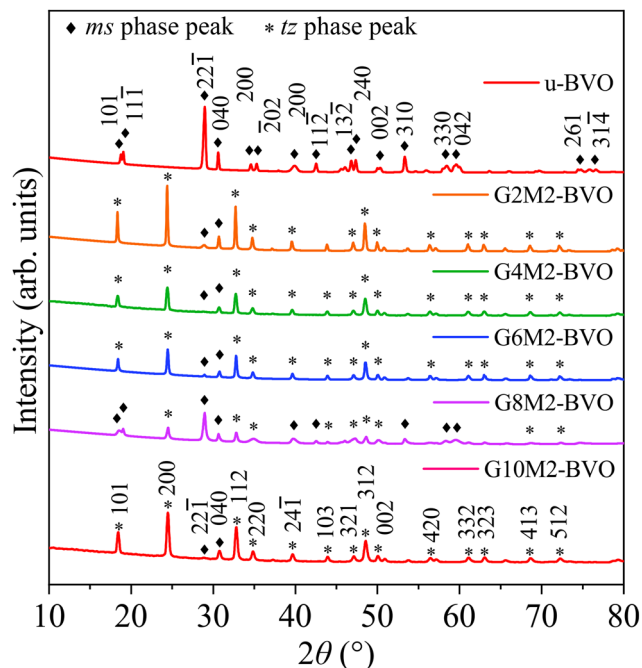

Fig. 1 Powdered XRD data of u-BVO, G2M2-BVO, G4M2-BVO, G6M2-BVO, G8M2-BVO, and G10M2-BVO. The ms and tz phases are marked with ♦ and *, respectively.

X-ray photoelectron spectrometer (XPS) operating with a monochromatic Al Kα source (1486.69 eV, 15 keV, 10 mA, 225 W). The binding energy of extraneous C-1s (284.8 eV) was used for XPS peak position calibration. The deep UV from a HeI (21.2 eV) source was used to record the valence band structure with an ultraviolet photoelectron spectrometer (UPS). The UV-vis diffuse reflectance spectroscopy (DRS) was facilitated by using a Shimadzu UV-2600i UV–vis–NIR spectrometer. The steady-state photoluminescence (PL) emissions were recorded in an F-7000 fluorescence spectrophotometer operating with a 150 W Xe lamp and photomultiplier tube voltage of 700 V. The UV-Vis absorption spectra of the dye degradation measurement were obtained with a Shimadzu UV-1900i spectrometer.

3. Results and discussion

3.1. Structural analysis

The XRD data of the undoped u-BVO and co-doped Gx%My%-BVO (x% = 2, 4, 6, 8 and 10; y% = 2) powder are shown in Fig. 1. A quantitative structural refinement of all samples was done based on the Rietveld method, see Fig. S2. Detailed crystallographic parameters from the Rietveld refinements are presented in Table S1. The pure ms phase (point group C_{2h}^6, space group $C2/c$ (15), JCPDS# 014-0688/ICSD#100602) is present in undoped u-BVO.[59] The (Gd^{3+}, Mo^{6+}) co-doping induced the coexistence of tz phase (point group C_{4h},[19] space group $I41/amd$ (141), and JCPDS# 14-0133/ICSD#100733) with ms.[28,60–62] This incomplete ms to tz phase transition due to Gd and Mo mono-doping is well-known in the existing literature.[41,43,58,63]

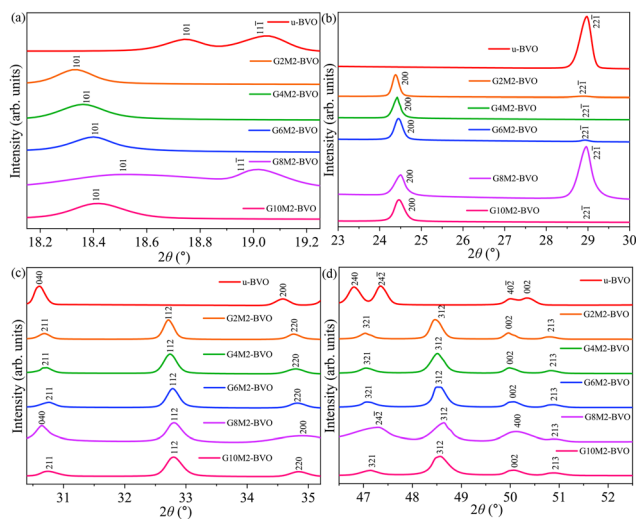**Fig. 2** XRD peak shifts in the 2θ range of (a) 18.2–19.2°, (b) 23–30°, (c) 30–35° and (d) 46–53° of u-BVO, G2M2-BVO, G4M2-BVO, G6M2-BVO, G8M2-BVO, and G10M2-BVO.

Now by comparing the normalized intensities $I_{\text{ms}}^{(22\bar{1})}$ and $I_{\text{tz}}^{(200)}$ of the most dominant diffraction peaks corresponding to the ms $(22\bar{1})$ and tz (200) planes as

$$\zeta_{\text{ms}} \ (\%) = \frac{I_{\text{ms}}^{(22\bar{1})}}{I_{\text{ms}}^{(22\bar{1})} + I_{\text{tz}}^{(200)}} \times 100, \tag{1}$$

the ms–tz phase mixing is quantified in Table S2.[63] The tz phase turned out to be the dominant one in all co-doped samples ($\zeta_{\text{ms}} < \zeta_{\text{tz}}$) except for the G8M2-BVO sample where the ζ_{ms} (64.21%) exceeds the ζ_{tz} (35.79%). The refinement correlation parameters R_{p} (5.89–12.1), R_{wp} (5.13–10.3), and R_{exp} (3.74–6.64) of all co-doped samples are in the satisfactory range, resulting in a goodness of fit parameter χ^2 in the high confidence range of 1.67–2.55.

The quantities like crystallite size D of the samples are derived from the full-width-half-maxima (fwhm) of the different XRD peaks (101), $(22\bar{1})$, and (200) using Debye–Scherrer's formula, along with other derivatives like defect density and strain as displayed in Table S3. It is evident that the dopants inhibit crystal growth, effectively reducing the crystallite size of the co-doped samples. Incorporating (Gd^{3+}, Mo^{6+}) dopants into the $BiVO_4$ lattice increases the defect density and strain as expected. The strain due to the dopant incorporation results in XRD peak shifts as shown in Fig. 2a–d. The slight discrepancies in ionic radii of the Gd^{3+} (105 pm) and Mo^{6+} (59 pm) dopants with their corresponding hosts Bi^{3+} (103 pm) and V^{5+} (54 pm) originate from strain in the $BiVO_4$ lattice. The small shift of the (101), (200), (112) and (312) peaks to higher angles indicates the presence of mild compressive strain due to the replacement of smaller host Bi^{3+} with the larger Gd^{3+} dopant incorporation.[39] Moreover, the intensity of the ms and tz phase-specific peaks varies following their relative percentages in the mixed phase. For example, the $(22\bar{1})$ peak of the ms dominates in u-BVO and G8M2-BVO, whereas the (200) dominates in other
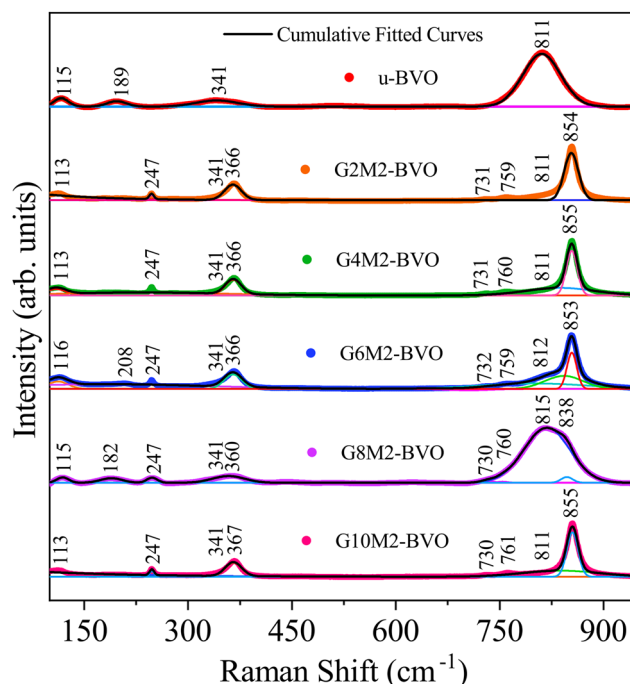

Fig. 3 Raman spectra of u-BVO, G2M2-BVO, G4M2-BVO, G6M2-BVO, G8M2-BVO, and G10M2-BVO measured at room temperature.

co-doped samples with tz as the dominant phase. The absence of the tetragonal scheelite phase can be substantiated by the higher pH (9) and hydrothermal reaction temperature (180 °C).[63–66] As the hydrothermal reaction progresses, the initial tz undergoes a gradual phase transition to ms for pH ≥ 7.[65,66] The presence of dopants inhibits the complete ms to tz transformation, and the mixed ms–tz phase prevailed in the co-doped sample.

3.2. Raman analysis

The irreducible representations of the $\Gamma_{\text{Raman}}^{\text{ms}} \ (C2/c) = 8A_g + 10B_g$ and $\Gamma_{\text{Raman}}^{\text{tz}} \ (I41/amd) = 2A_{1g} + 4B_{1g} + B_{2g} + 5E_g$ define the Raman active modes of the ms and tz phases, respectively.[18,67,68] The room temperature Raman spectra of all samples are presented in Fig. 3 and the corresponding mode assignment is displayed in Table S4. The phase-independent external lattice modes (translation or rotation) of $[VO_4]^{3-}$ appeared near 115(2) (B_g), 190(2) (A_g) and 208(2) (A_g) cm^{-1}.[30,59] In all co-doped samples, symmetric stretching (A_g) of the tz phase produced the Raman band at 247(2) cm^{-1}. The bands near 341(2) (B_g) and 366(2) (A_g) cm^{-1} can be ascribed to asymmetric and symmetric deformation of the $[VO_4]^{3-}$ tetrahedron of the ms phase.[69] The Raman band of the ms phase around 731(2) cm^{-1} is observed due to symmetric stretching of the V–O bond. The bands near 759(2) and 854(2) cm^{-1} represent asymmetric (B_g) stretching and symmetric (A_g) bending vibration of the V–O bond in the tz phase. The Raman band near 810(2) cm^{-1} is observed owing to the characteristic symmetric stretching of the V–O bond in the ms phase.[70] The ms phase purity of the undoped u-BVO was corroborated from the Raman bands near 325(2), 367(2), 731(2), and 811(2) cm^{-1}. The coexistence of these ms bands along
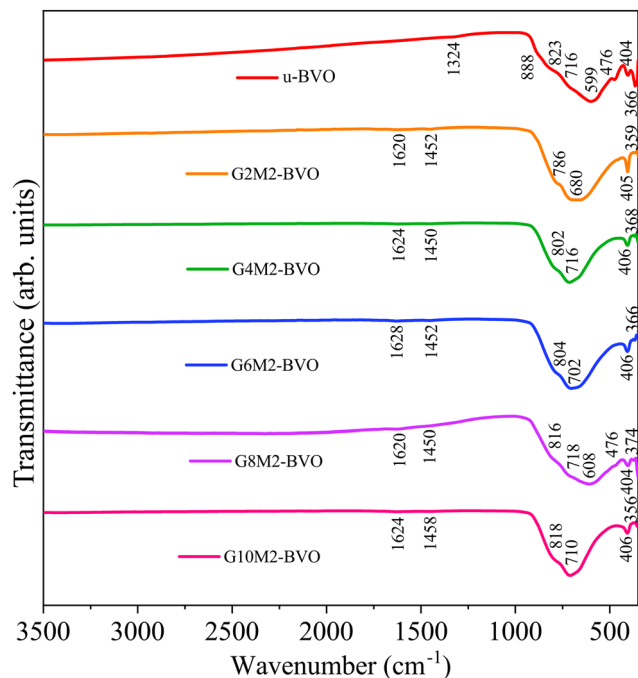
Fig. 4 FTIR absorptions of u-BVO, G2M2-BVO, G4M2-BVO, G6M2-BVO, G8M2-BVO, and G10M2-BVO.

with tz bands near 247(2), 759(2), and 854(2) cm^{-1} confirmed the mixed ms–tz phase in all (Gd^{3+}, Mo^{6+}) co-doped samples.

3.3. Fourier transform infrared spectroscopy

The FTIR spectra (Fig. 4) of all as-synthesized nanoparticles are assigned to relevant atomic bond vibrations (Table S5). The symmetric stretching vibration of Bi–O stems from the IR bands near 360(4) and 404(4) cm^{-1}.[71] The absorptions near 476(4) and 600(4) cm^{-1} for u-BVO and G8M2-BVO are owing to [VO$_4$]$^{3-}$ tetrahedral symmetric bending and asymmetric stretching vibration of the V–O bond, respectively.[72] The asymmetrical stretching of the [VO$_4$]$^{3-}$ unit appeared near 720(4) cm^{-1} in all samples.[73–76] The IR band near 823(4) cm^{-1} can be assigned to the stretching vibration of V–O. The (Gd^{3+}, Mo^{6+}) co-doping slightly shifts this 823(4) cm^{-1} mode to a lower wavenumber due to a change in V–O bond length induced by dopants.[39] A weak IR absorption is detected near 888(4) cm^{-1} in the u-BVO, corresponding to symmetric stretching of the V–O. The extraneous CO$_2$ adsorbed in the samples during material processing stemmed from the minor IR absorption of the C=O bond near 1320(4)–1450(4) cm^{-1}.[35] The bending vibration of the O–H in the H$_2$O molecule appeared at 1620(4) cm^{-1}.[43,77,78] This tendency of water adsorption at the surface can be favorable to the photocatalytic activity.[79]

3.4. Surface morphology and elemental analysis

The u-BVO morphology in Fig. 5(a) displayed connected buckhorn-shaped nanorods with an average diameter of 650 nm.[22,45,80] The (Gd^{3+}, Mo^{6+}) co-doping transformed the surface morphology to an irregular agglomeration of randomly shaped nanorods (Fig. 5b–e, f) with an average size lying in the range of 80–130 nm. The high pH = 9 during synthesis randomizes nanoparticle shapes across all co-doped samples.[28,41,62,81] The nanoparticle agglomeration can be ascribed to sizable surface energies in the hydrothermal process.[82] For the G8M2-BVO sample with a dominant ms phase among the ms–tz mixture, the uniform compact agglomeration may have hindered the intra-agglomerate pore
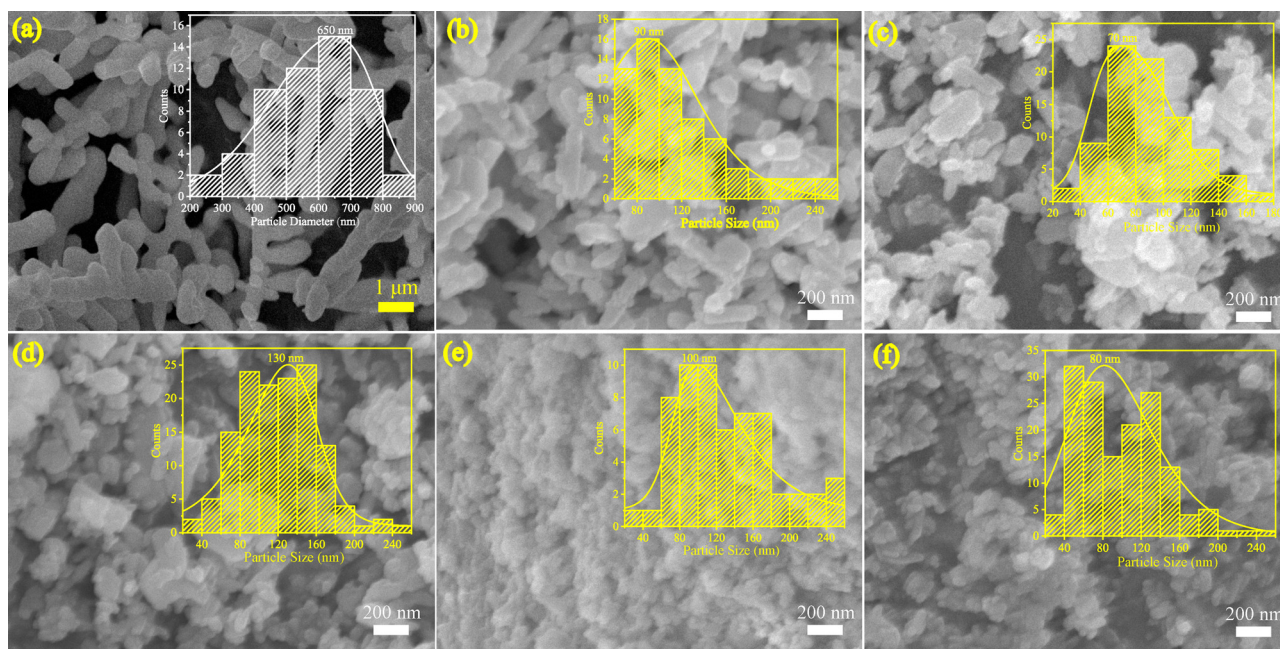

Fig. 5 FESEM micrographs of (a) u-BVO, (b) G2M2-BVO, (c) G4M2-BVO, (d) G6M2-BVO, (e) G8M2-BVO, and (f) G10M2-BVO with particle size histograms superimposed.
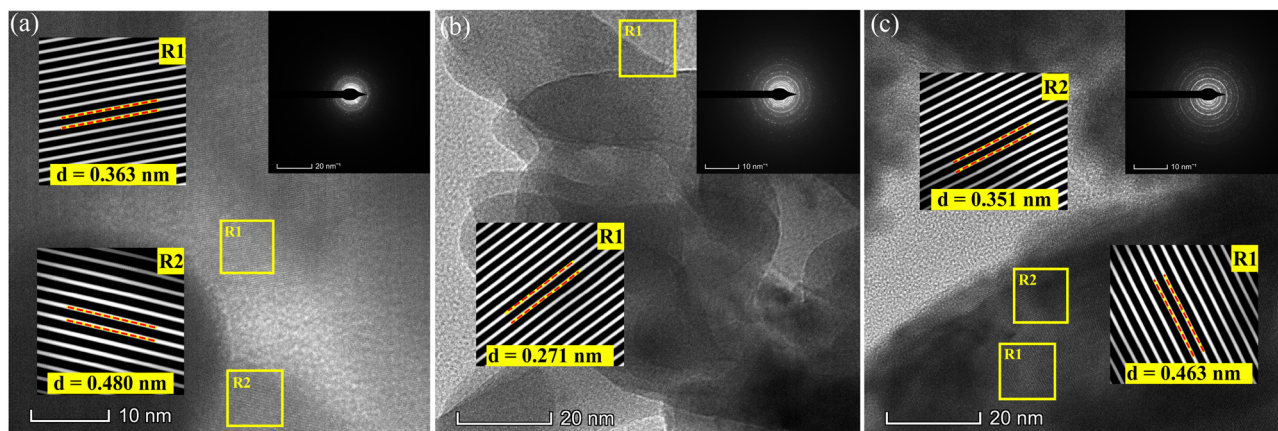
Fig. 6 HRTEM micrographs and SEAD images (inset) of (a) G6M2–BVO, (b) G8M2–BVO, and (c) G10M2–BVO.

formation.[83] The desired elemental identifications of all the samples were confirmed by the EDX spectra (Fig. S3 and Table S6). The EDX spatial scans of u-BVO and co-doped G6M2-BVO, G8M2-BVO, and G10M2-BVO (Fig. S4–S7) corroborate the desired homogeneity of the host (Bi, V, and O) and dopants (Gd, Mo) across the samples.[84,85] This excludes the possibility of spurious effects due to dopant agglomeration in the as-synthesized samples.[43,86–92]

Fig. 6a–c presents the HRTEM, and SAED measurements of the (Gd, Mo) co-doped G6M2-BVO, G8M2-BVO, and G10M2-BVO samples, respectively. The textured morphology of the polycrystalline sample formed concentric circles with non-uniform intensities in the SAED patterns. The lattice fringes of the ms and tz phase are marked with rectangular yellow boxes R1 and R2 on HRTEM, and a magnified view is presented in the insets. The lattice fringes with a
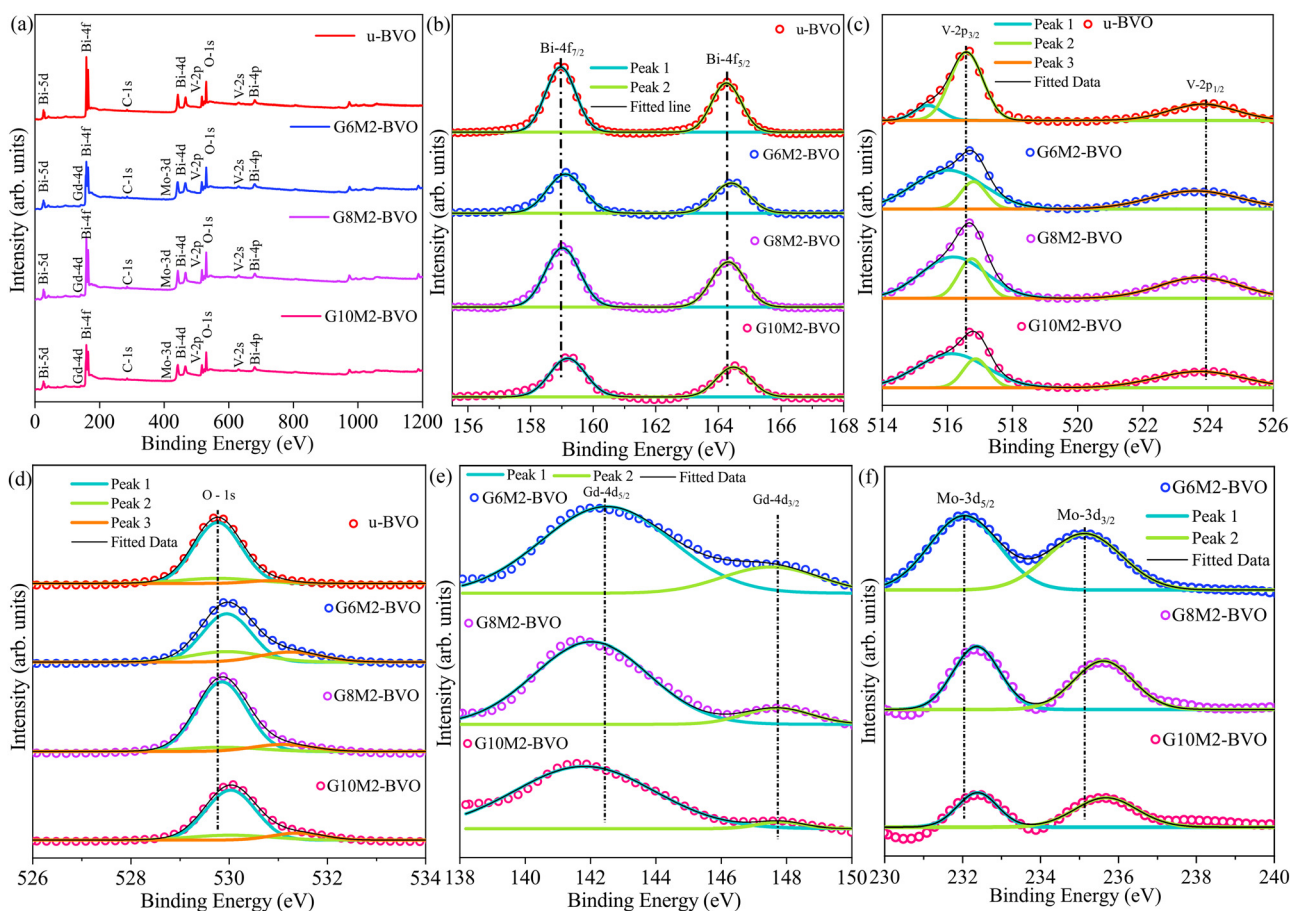

Fig. 7 (a) XPS full survey spectra and core level spectra of (b) Bi-4f, (c) V-2p, (d) O-1s, (e) Gd-4d, and (f) Mo-3d of u-BVO, G6M2–BVO, G8M2–BVO, and G10M2–BVO.

d-spacing of 0.363 nm and 0.480 nm in Fig. 6a can be ascribed to the (200) and (101) planes of the tz and ms phases, respectively. The *d*-spacing of 0.17 nm in the R1 region as displayed in Fig. 6b inset corresponds to the (200)/(112) crystallographic planes of the ms/tz phases. The ms (111) (R1) and tz (113) (R2) planes are detected in G6M2-BVO (Fig. 6c) with *d*-spacings of 0.463 and 0.351 nm, respectively. Overall, the TEM analysis confirmed the presence of mixed ms/tz phases along with the desired crystallographic planes in the co-doped samples.

3.5. Chemical state analysis

The XPS survey spectra in Fig. 7(a) corroborated the Bi, V, O, Gd, and Mo as the desired constituent elements in the

Fig. 8 The UV-vis absorbance of u-BVO, G2M2–BVO, G4M2–BVO, G6M2–BVO, G8M2–BVO, and G10M2–BVO derived from DRS.

respective samples. The adventitious C-1s peak at a binding energy of 248.8 eV is present in all samples. The high-resolution core level Bi-4f spectra of u-BVO in Fig. 7(b) revealed Bi-4f$_{7/2}$ and Bi-4f$_{5/2}$ XPS lines at 158.9 and 164.3 eV, which are consistent with the Bi^{3+} oxidation state.[93–95] The blue shift of the binding energies of these two peaks increases with the Gd concentration, but their splitting due to spin–orbit coupling (SOC) remains ∼5.4 eV. The V-2p core spectra of u-BVO in Fig. 7(c) display ∼7.4 eV SOC driven splitting of the V-2p$_{3/2}$ and V-2p$_{1/2}$ lines at 516.5 and 523.9 eV, respectively, corroborating the V^{5+} oxidation state.[96] The (Gd, Mo) co-doping introduced asymmetry and blue-shift in the V-2p$_{3/2}$ peak. The distinct symmetrical peak of u-BVO at 529.7 eV in Fig. 7(d) corresponds to the O-1s XPS peak originating from the lattice O of the BVO crystal.[97] The weak XPS line at 530.9 eV is ascribed to extraneous OH formed on the surface of the sample.[81] The (Gd^{3+}, Mo^{6+}) dopants blue shift the O-1s signal, enhance the XPS signal of the extraneous OH, and make it most prominent for the G6M2-BVO sample. The Gd-4d core level in the G6M2-BVO sample in Fig. 7(e) exhibits Gd-4d$_{5/2}$ and Gd-4d$_{3/2}$ XPS lines occurring at binding energies of 142.5 and 147.7 eV, subjected to 5.2 eV splitting due to SOC.[58] This matches the Gd^{3+} oxidation state in Gd$_2$O$_3$, implicating successful Gd dopant incorporation as it binds with O atoms.[98] The Gd-4d core levels are red-shifted with increasing Gd concentrations. The XPS core level of Mo-3d in the G6M2-BVO sample in Fig. 7(f) have undergone 3 eV SOC splitting of the Mo-3d$_{5/2}$ and Mo-3d$_{3/2}$ XPS lines located at 232.1 and 235.1 eV, respectively, conforming with the Mo^{6+} oxidation state.[89,99,100] The Mo-3d XPS lines get blue-shifted as more Gd is incorporated into the lattice. In general, these XPS binding energy shifts can be ascribed to different electronegativities of the hosts (Bi^{3+}, V^{5+}) and dopants (Gd^{3+}, Mo^{6+}) as well as dopant-induced changes in the local coordination environments of the host atoms.[89,101,102]
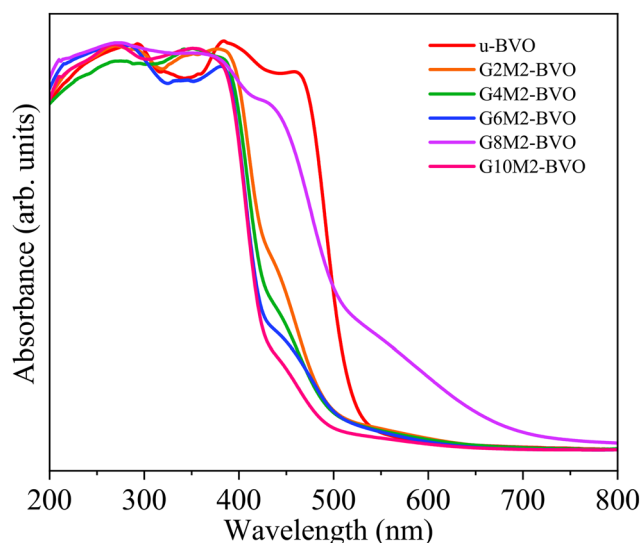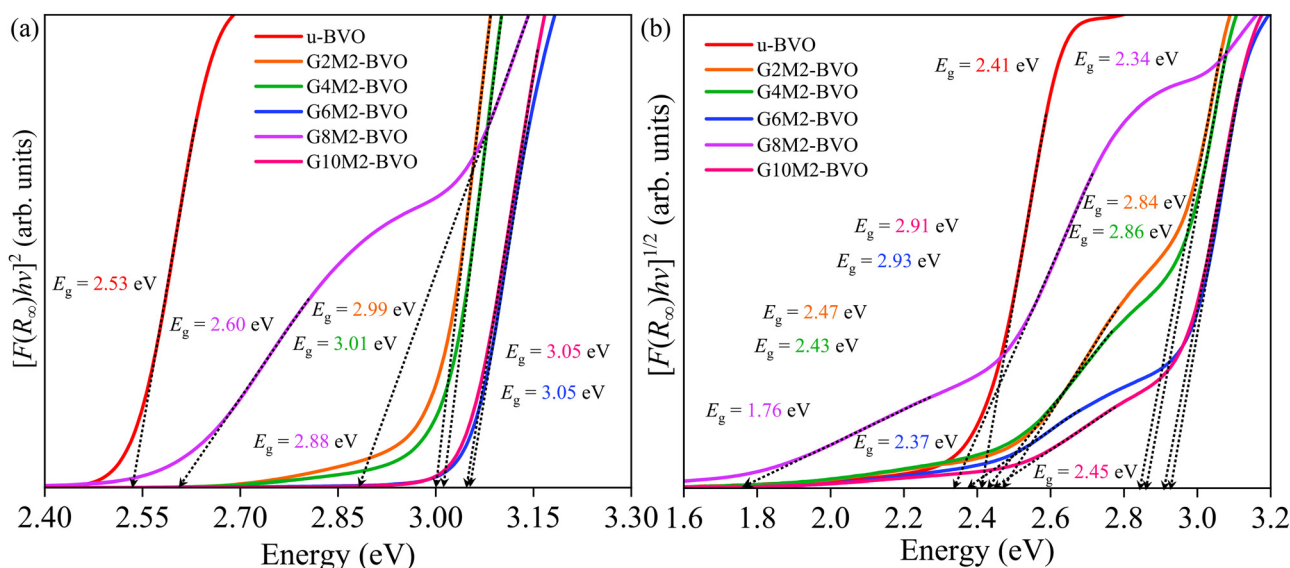

Fig. 9 (a) Direct and (b) indirect band gap in the Tauc plot of u-BVO, G2M2–BVO, G4M2–BVO, G6M2–BVO, G8M2–BVO, and G10M2–BVO, derived from DRS.

3.6. UV-vis spectroscopy

The UV-vis absorbances (Fig. 8) were derived from measured diffuse reflectance using the Kubelka–Munk function $F(R_\infty)$. The undoped u-BVO possesses a single-slope edge, whereas the co-doped samples display edges with two different slopes. The steeper edge of the G2M2-BVO co-doped sample was blue-shifted by 60 nm from that of u-BVO. With increasing Gd concentrations of 4 and 6%, the steeper edges of the co-doped G4M2-BVO and G6M2-BVO samples were blue-shifted by ~10 nm with each increment. No palpable shift in the absorption edge was observed between G10M2-BVO and G6M2-BVO. The exception occurred in G8M2-BVO, where the steep absorption edge stayed close to that of u-BVO, and an absorption tail appeared in the longer wavelength region. This represents Urbach tails resembling the sub-band gap optical absorption, originating from defect states introduced by the (Gd^{3+}, Mo^{6+}) dopants in the band gap of $BiVO_4$.[103,104] The Tauc procedure was employed to evaluate the E_g, which is related to photon energy $h\nu$ by the $F(R_\infty)$ as:

$$[F(R_\infty)h\nu]^{1/\gamma} = A(h\nu - E_g), \quad (2)$$

where A is a constant and γ defines the nature of the electronic transition (indirect: $\gamma = 2$ and direct: $\gamma = 1/2$). The direct Tauc plots of all samples in Fig. 9(a) revealed an E_g of 2.53 eV for the u-BVO. The introduction of (Gd = 2%, Mo = 2%) dopants in G2M2-BVO increased the direct E_g to 2.99 eV. The further increments in Gd dopant concentration in G4M2-BVO (3.01 eV), G6M2-BVO (3.05 eV), G8M2-BVO (2.88 eV), and G10M2-BVO (3.05 eV) seem to have minor effects on direct E_g. For G8M2-BVO, an additional E_g with a lower energy of 2.60 eV is observed. Next, the indirect Tauc plots are displayed in Fig. 9(b). The u-BVO possessed an indirect E_g of 2.41 eV. For all co-doped samples, a pair of E_g is observed, one of which lies close to that of u-BVO, and the other is located higher in energy (except for G8M2-BVO, where the E_g = 1.76 eV) range is 2.84–2.93 eV. The estimated direct and indirect E_g of all samples, along with their corresponding electronic transitions, were displayed in Table S7. The E_g = 1.76 eV can be ascribed to the electronic transition from the Mo-4d to O-2p states. The E_g lying
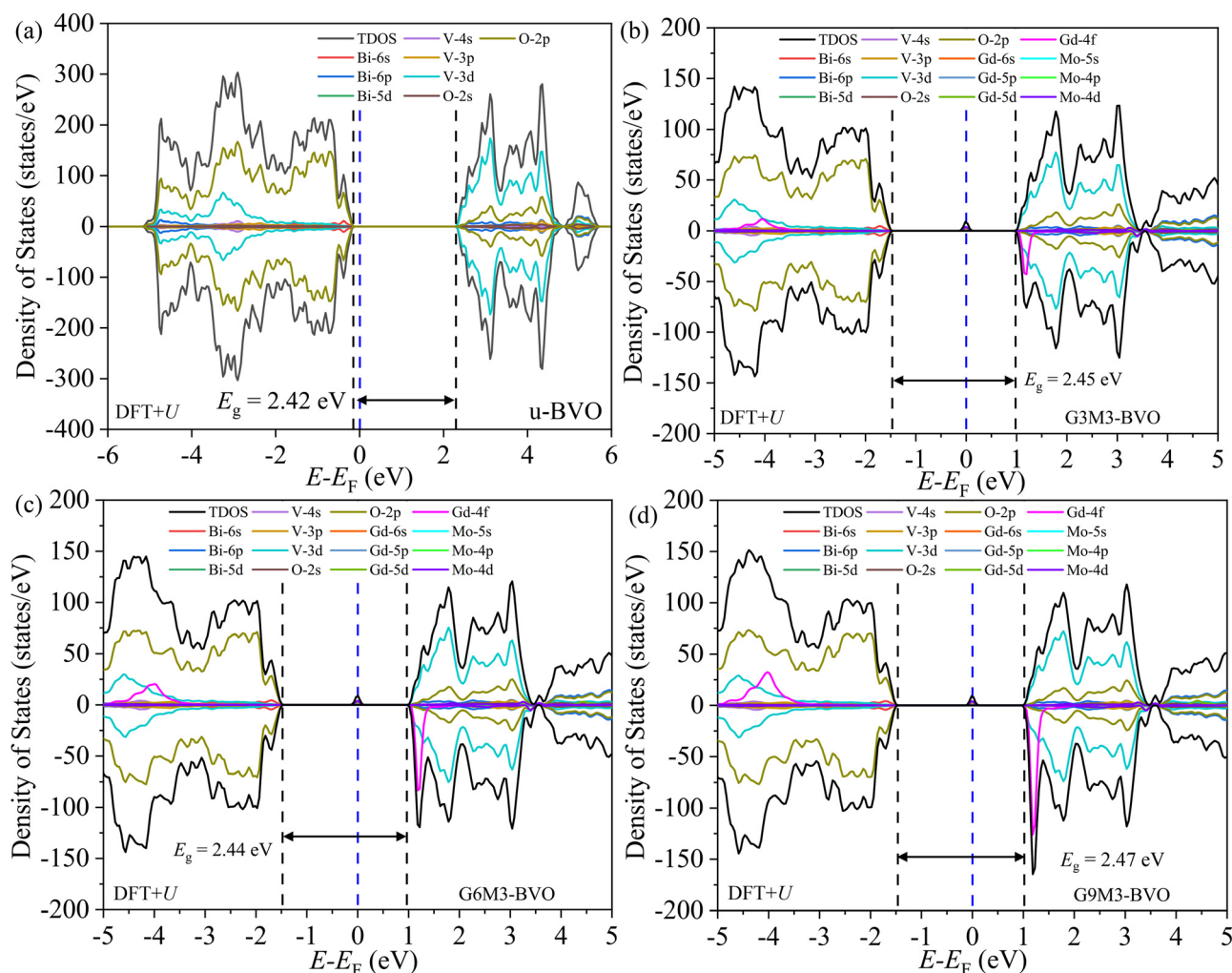

Fig. 10 Total density of states (TDOS) and its projections on different atomic orbitals of (a) u-BVO, (b) 3.125% Gd and 3.125% Mo co-doped G3M3-BVO, (c) 6.25% Gd and 3.125% Mo co-doped G6M3-BVO, and (d) 9.375% Gd and 3.125% Mo co-doped G9M3-BVO using DFT+U XCF. The Fermi level E_F is set as the zero of energy.

in the 2.41–2.59 eV range corresponds to electronic transitions from the V-3d states of the conduction band (CB) to the O-2p states of the valence band (VB). The electronic transitions between impurity states like Mo-4d near CB and Gd-4f in VB stemmed from E_g in the range of 2.84–3.05 eV.

3.7. Electronic structure analysis

The total density of states (TDOS) and its orbital projections of the u-doped and (Gd, Mo) co-doped BVO supercell were simulated using optimum DFT+U XCF. The u-BVO supercell yields an E_g of 2.42 eV (Fig. 10a). The states near the valence band maxima (VBM) originate from O-2p and Bi-6s hybridization. The presence of Bi-5d states near the VBM and conduction band minima (CBM) is insignificant. The states near the CBM stemmed from hybridization of V-3d, Bi-6p, and O-2p orbitals. The V-3d has undergone tetrahedral crystal-field induced splitting. In the case of (Gd^{3+}, Mo^{6+}) co-doping, in addition, two distinct features became evident: (i) Gd-4f spin down states appeared near the CBM and take part in hybridization with Bi-6p, V-3d, and O-2p; (ii) shallow up-spin impurity states (closer to CBM) stemmed from the hybridization of Mo-4d, O-2p and V-3d orbitals. These trap states can capture photogenerated electrons, retarding their recombination with holes, effectively prolonging their lifetime, and thereby improving the photocatalytic performance.[40,102,105,106] For the co-doped supercells, where the Gd dopant concentration varies as 3.125, 6.25, and 9.375% while keeping the Mo concentration fixed at 3.125% (Fig. 10b–d), the VB and CB edge positions remain essentially the same and the E_g remains fixed at $\sim$2.45 eV. The Gd-4f orbital contribution near the CBM gradually increases with the Gd dopant concentration.

Now we probe the valence band structure of u-BVO and (Gd^{3+}, Mo^{6+}) co-doped BiVO$_4$ nanoparticles by targeting the valence electrons with a HeI source in UPS measurements. The photoelectron intensity is plotted against the binding energy (Fig. 11) near the Fermi level (E_F). The dotted circle encloses very similar rising edges from E_F for undoped and co-doped samples. The linear extrapolations of these rising edges on the binding energy axis yield a similar VB edge energy of $\sim$0.12 eV. This corroborates the fact that the VBM energy remains fixed as we introduce (Gd^{3+}, Mo^{6+}) dopants, consistent with our DFT simulation.

3.8. Steady state photoluminescence

The photo-excited EHP recombination generates PL emission, and hence its intensity is correlated with the photocatalytic performance of the material.[107,108] Generally, higher PL intensity indicates higher EHP recombination, leading to photocatalytic performance deterioration.[109–113] The room temperature steady-state PL emissions of all samples are presented in Fig. 12 with an excitation wavelength λ_{ex} at 270 nm. The electrons from the CB (V-3d states) make a downward radiative transition to holes in the VB (Bi-5d and O-2p hybridized states) of undoped u-BVO, generating the PL emission at $\sim$582 nm with a fwhm of $\sim$75 nm.[35,80,114,115] The PL emission peaks are blue-shifted to 469–508 nm for the (Gd^{3+}, Mo^{6+}) co-doped samples. This blue-
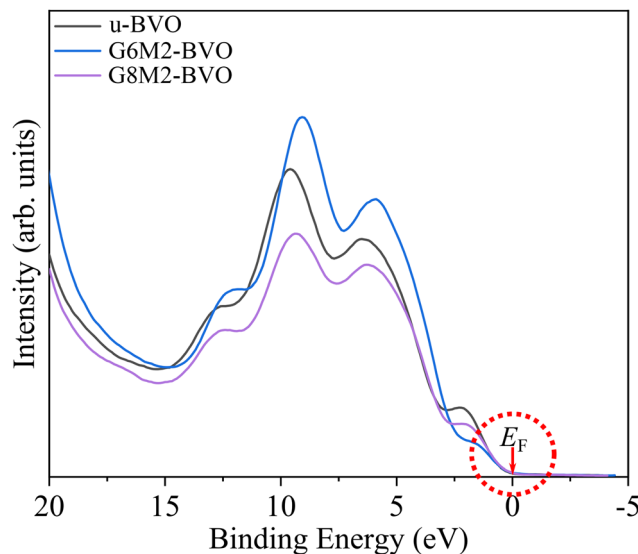
Fig. 11 Ultraviolet photoelectron spectra of the valence band of u-BVO, G6M2-BVO, and G8M2-BVO near the Fermi energy E_F.

shift is consistent with the band gap increment due to co-doping in the BiVO$_4$ crystal as presented in Section 3.6. The PL intensity gradually decreases with increasing Gd content from 2 to 8%, inferring a reduction of radiative EHP recombination. The observed red shift in PL emission for G8M2-BVO ($\sim$508 nm with a fwhm of $\sim$96 nm) compared to other co-doped samples can be ascribed to extrinsic radiative recombination from Urbach tail states at longer wavelengths. The PL intensity peak reaches a maximum for G10M2-BVO at $\sim$464 nm with a fwhm of 97 nm among all co-doped samples. This enhancement in PL emission can be attributed to the higher EHP recombination *via* the defect states.
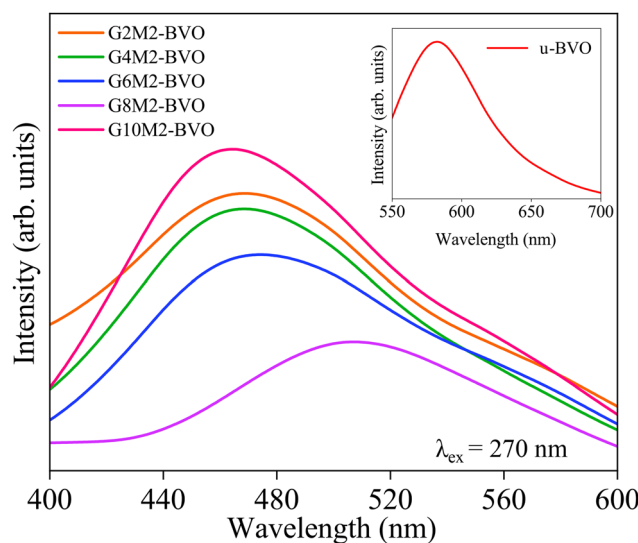
Fig. 12 Steady-state room temperature photoluminescence of u-BVO (inset), G2M2-BVO, G4M2-BVO, G6M2-BVO, G8M2-BVO, and G10M2-BVO.
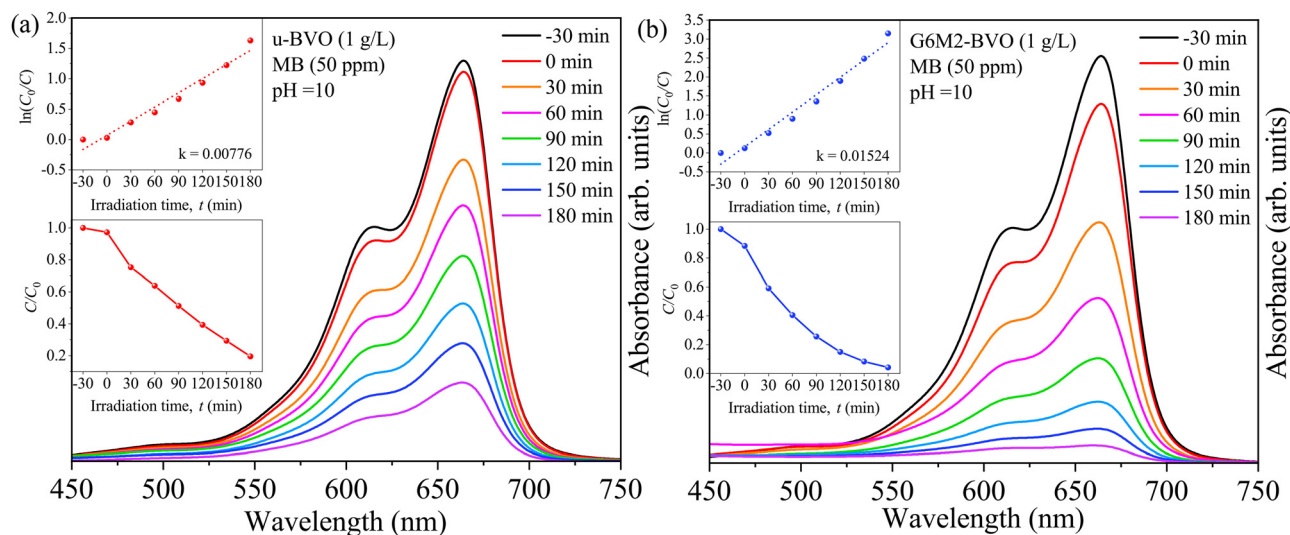
Fig. 13 The photocatalytic degradation measurements from UV-Vis absorption spectra of (a) u-BVO and (b) G6M2-BVO photocatalysts (1 g L^{-1}) with 50 ppm MB dye.

3.9. Photocatalytic performance analysis

The photocatalyst induces decolorization of toxic dyes by annihilating their chromophoric structure under optical illumination. Fig. 13(a) displays the UV-vis absorption measurements, characterizing the MB dye degradation by u-BVO. The degradation in dark conditions due to surface adsorption is nominal. As the photocatalyst degrades the MB dye, the intensity of its characteristic 665 nm peak gradually diminishes over irradiation time.[116–119] By plotting the ratio of C to C_0, where C_0 and C stand for initial and time-specific dye concentrations, the photocatalytic efficiency was evaluated to be 81% (inset). In addition, a pseudo-first-order $\ln(C_0/C) = kt$ model was used to capture the reaction kinetics, and the estimated reaction rate constant k turned out to be 0.00776 min^{-1}. The pure ms phase of u-BVO with a direct band gap of 2.53 eV can be attributed to this visible photocatalytic activity.[120] Moreover, the buck-horn type morphology of the u-BVO may have enhanced electron–hole separation, desired in the efficient photocatalytic mechanism.[80,121] For the sake of brevity, the detailed photocatalytic degradation measurements of the co-doped sample are presented in Fig. S8 and S9 and the results are summarized in Table S8. The (Gd^{3+}, Mo^{6+}) co-doping of BiVO$_4$ improved the photocatalytic efficiencies. The best-performing co-doped G6M2-BVO (Fig. 13b) obtained 96% efficiency over 180 min of optical exposure with a reaction rate as high as 0.01524. Several factors can be ascribed to this photocatalytic performance enhancement due to co-doping. The 2% Mo^{6+} donor dopant present in V^{5+} acts as a shallow donor and enhances stability, electron conductivity, diffusion length, mobility, and EHP separation efficiency.[28] The isovalent Gd^{3+} dopant in Bi^{3+} can provide the desired distortion in the monoclinic structure, effectively reducing the hole's effective mass to enhance its mobility.[38,122] Moreover, the Gd^{3+} at the surface of BVO can act as a charge trapping center to facilitate the charge transfer in

photocatalytic reactions.[120] Notably, the Gd^{3+} dopant inflates carrier mobility and lifetime in BVO, effective in preventing unwanted EHP recombinations. This conjecture is supported by the reduced PL emission of the G6M2-BVO, presented in Section 3.8.

3.10. Photocatalytic mechanism

During the photocatalytic reaction, optical energy $h\nu$ excites electrons from the VB to CB of the photocatalyst, creating holes in the VB. These EHPs can produce reactive oxygen species, facilitating the redox reactions to degrade the MB dye. The photogenerated e$^-$ in CB may successively reduce dissolved O$_2$ to H$_2$O$_2$ and hydroxyl ($^\bullet$OH) radicals. The photogenerated h$^+$ react with adsorbed H$_2$O on the surface of the photocatalyst to supply $^\bullet$OH radicals. A tentative reaction pathway for MB dye
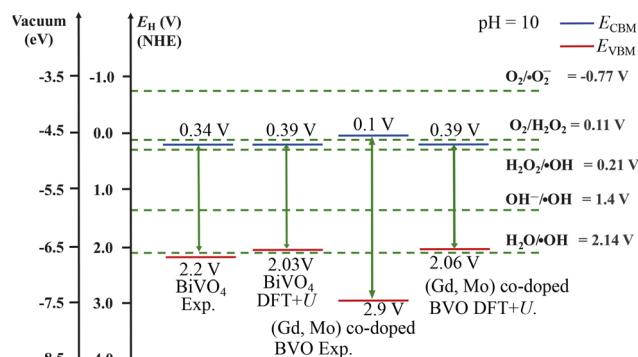

Fig. 14 Experimental (Exp.) and DFT+U derived conduction E_{CBM} and valence E_{VBM} band-edge positions of undoped and (Gd, Mo) co-doped BiVO$_4$ with respect to relevant photocatalytic redox reaction potentials at pH = 10.

degradation with these EHP-generated $^\bullet$OH is as follows:

$$BiVO_4 + h\nu \rightarrow BiVO_4 + 2e^- + h^+$$

$$2H^+ + O_2 + 2e^- \rightarrow H_2O_2$$

$$H_2O_2 + H^+ + e^- \rightarrow {}^\bullet OH + H_2O \qquad (3)$$

$$H_2O + h^+ \rightarrow H^+ + {}^\bullet OH$$

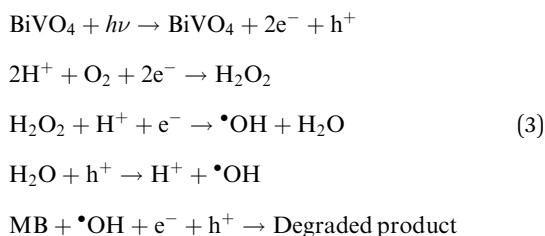$$MB + {}^\bullet OH + e^- + h^+ \rightarrow Degraded\ product$$

Table S9 summarizes the relevant chemical reactions and their corresponding redox potentials at different pH levels. To probe the reaction potential, the Mulliken electronegativity χ of $BiVO_4$ was estimated to be 6.04 eV, as the geometric mean of the absolute electronegativities of Bi (4.25 eV), V (3.60 eV), and O (7.54 eV). Assuming free electron energy of $E_e = 4.44$ eV in the normal hydrogen electrode (NHE) scale, VBM and CBM edge energies can be estimated as

$$E_{VBM} = \chi - E_e + \frac{1}{2}E_g \qquad (4)$$

$$E_{CBM} = E_{VBM} - E_g \qquad (5)$$

By using the experimental and DFT+U derived E_g, the VBM and CBM edge energies E_{VBM} and E_{CBM} were obtained. Fig. 14 presents the E_{VBM} and E_{CBM} band-edge locations of undoped and (Gd^{3+}, Mo^{6+}) co-doped $BiVO_4$ along with the redox potentials of O_2/H_2O_2 and $H_2O/^\bullet OH$ at pH = 10. The E_{VBM} and E_{CBM} straddled these photocatalytic redox potentials, corroborating the proposed photocatalytic MB dye degradation by the (Gd^{3+}, Mo^{6+}) co-doped $BiVO_4$ photocatalyst.

4. Conclusion

We report a surfactant-free hydrothermal synthesis of (Gd^{3+}, Mo^{6+}) co-doped $BiVO_4$ nanoparticles. The incorporation of Gd and Mo dopants gradually changes the ms–tz phase mixing proportions of the $Bi_{1-x}Gd_xV_{1-y}Mo_yO_4$ samples. The Raman peaks further corroborated the co-existence of mixed ms–tz phase in the co-doped $BiVO_4$. Co-doping induced a morphological evolution in $BiVO_4$, transforming it from buckhorn-shaped nanorods to rectangular nanorods and finally to irregular nanoparticles. High resolution transmission electron microscopy revealed the desired crystallinity of the co-doped nanoparticles. The desired Bi^{3+}, V^{5+}, O^{2-}, Gd^{3+}, and Mo^{6+} oxidation states in the as-synthesized undoped and co-doped samples were confirmed from X-ray photoelectron spectroscopy. The (Gd^{3+}, Mo^{6+}) co-doping essentially left the valence band edge energy unchanged, as revealed from ultraviolet photoelectron spectroscopy and DFT+U simulations. The co-doping induced multiple band gaps lying in the range of 2.41–3.05 eV as per the DRS due to multiple electronic transitions among different states, supported by DFT+U derived density of states simulations. The suppression of radiative recombination of photogenerated carriers was evident due to (Gd^{3+}, Mo^{6+}) co-doping in steady-state photoluminescence. The best-performing

$Bi_{0.94}Gd_{0.06}V_{0.98}Mo_{0.02}O_4$ photocatalyst nanoparticles degraded 50 ppm methylene blue dye in 180 min with 0.01524 min^{-1} reaction rate. The band edges straddled the desired photocatalytic redox potentials for driving the relevant reactions. This superior photocatalytic performance of (Gd^{3+}, Mo^{6+}) co-doped $BiVO_4$ may have originated synergistically from mixed ms–tz phase distortion, higher optical absorption, high surface-to-volume ratio of the nanoparticles, favorable band edge alignment, and reduced radiative recombinations.

Author contributions

I. A. planned and supervised the entire project, acquired the research funding, and wrote the original article. N. E. and M. R. H. contributed equally. N. E. and M. R. H. prepared all samples and performed the photocatalytic measurements. M. N. I. K. and H. N. helped with XRD, FTIR, and TEM measurements. M. S. B., D. I., and S. J. facilitated the SEM, FESEM, EDX, and Raman measurements. S. A. J. and U. S. A. performed the XPS measurements and analysis. N. E., M. R. H., and M. Z. H. performed the PL measurements. K. S. H. provided DRS measurements support. S. S. N., Q. S. H., and I. A. performed the DFT simulations. N. E., M. R. H., and I. A. performed the data curation.

Conflicts of interest

The authors declare no competing interests.

Data availability

The data that support the findings of this study are available from the corresponding author upon reasonable request.

The data supporting this article have been included as part of the supplementary information (SI). Supplementary information: a 2 × 2 × 2 supercell structure, detailed experimental XRD peak analysis with Rietveld refinement, Raman analysis, FTIR peak assignments, elemental and spatial EDX analysis, photocatalytic dye degradation measurements, and reaction potentials of undoped and (Gd^{3+}, Mo^{6+}) co-doped $BiVO_4$. See DOI: **https://doi.org/10.1039/d5ma01129a**.

Acknowledgements

References

1 M. F. Lanjwani, M. Tuzen, M. Y. Khuhawar and T. A. Saleh, Trends in photocatalytic degradation of organic dye pollutants using nanoparticles: A review, *Inorg. Chem. Commun.*, 2024, **159**, 111613.

2 S. Heckel, M. Wittmann, M. Reid, K. Villa and J. Simmchen, An account on $BiVO_4$ as photocatalytic active matter, *Acc Mater. Res.*, 2024, **5**(4), 400–412.

3 S. Khan, T. Noor, N. Iqbal and L. Yaqoob, Photocatalytic dye degradation from textile wastewater: a review, *ACS Omega*, 2024, **9**(20), 21751–21767.

4 F. Lalrindiki, N. P. Singh and N. M. Singh, A review of synthesis, photocatalytic, photoluminescence and antibacterial properties of bismuth vanadate-based nanomaterial, *Inorg. Chem. Commun.*, 2024, **168**, 112846.

5 S. Lotfi, M. E. Ouardi, H. A. Ahsaine and A. Assani, Recent progress on the synthesis, morphology and photocatalytic dye degradation of $BiVO_4$ photocatalysts: A review, *Catal. Rev.*, 2024, **66**(1), 214–258.

6 B. Guan, J. Chen, Z. Li, Z. Zhuang, Y. Chen and Z. Ma, *et al.*, Review on synthesis, modification, morphology, and combination of $BiVO_4$-based catalysts for photochemistry: status, advances, and perspectives, *Energ Fuel*, 2023, **38**(2), 806–853.

7 J. Liu, B. Li, L. Kong, Q. Xiao and S. Huang, Surfactants-assisted morphological regulation of $BiVO_4$ nanostructures for photocatalytic degradation of organic pollutants in wastewater, *J. Phys. Chem. Solids*, 2023, **172**, 111079.

8 H. H. Naing, K. Wang, Y. Li, A. K. Mishra and G. Zhang, Sepiolite supported $BiVO_4$ nanocomposites for efficient photocatalytic degradation of organic pollutants: Insight into the interface effect towards separation of photogenerated charges, *Sci. Total Environ.*, 2020, **722**, 137825.

9 M. S. Mansha, T. Iqbal, M. Farooq, K. N. Riaz, S. Afsheen and M. S. Sultan, *et al.*, Facile hydrothermal synthesis of $BiVO_4$ nanomaterials for degradation of industrial waste, *Heliyon*, 2023, **9**(5), e15978.

10 X. Li, Z. Wang, A. Sasani, A. Baktash, K. Wang and H. Lu, *et al.*, Oxygen vacancy induced defect dipoles in $BiVO_4$ for photoelectrocatalytic partial oxidation of methane, *Nat. Commun.*, 2024, **15**(1), 9127.

11 S. Wang, C. Li, Y. Qi, J. Zhang, N. Wang and M. Liu, *et al.*, Etched $BiVO_4$ photocatalyst with charge separation efficiency exceeding 90%, *Nat. Commun.*, 2025, **16**(1), 3776.

12 C. Regmi, Y. K. Kshetri, S. K. Ray, R. P. Pandey and S. W. Lee, Utilization of visible to NIR light energy by Yb^{3+}, Er^{3+} and Tm^{3+} doped $BiVO_4$ for the photocatalytic degradation of methylene blue, *Appl. Surf. Sci.*, 2017, **392**, 61–70.

13 K. Lv, D. Wan, D. Zheng, Y. Qin and Y. Lv, Enhancement of visible light photocatalytic activity of $BiVO_4$ by polypyrrole modification, *J. Alloys Compd.*, 2021, **872**, 159597.

14 F. F. Abdi, T. J. Savenije, M. M. May, B. Dam and R. van de Krol, The origin of slow carrier transport in $BiVO_4$ thin film photoanodes: A time-resolved microwave conductivity study, *J. Phys. Chem. Lett.*, 2013, **4**(16), 2752–2757.

15 S. Lardhi, L. Cavallo and M. Harb, Determination of the intrinsic defect at the origin of poor H_2 evolution performance of the monoclinic $BiVO_4$ photocatalyst using density functional theory, *J. Phys. Chem. C*, 2018, **122**(32), 18204–18211.

16 G. L. Li, First-principles investigation of the surface properties of fergusonite-type monoclinic $BiVO_4$ photocatalyst, *RSC Adv.*, 2017, **7**(15), 9130–9140.

17 C. Regmi, Y. K. Kshetri, D. Dhakal, J. K. Sohng, F. Rosei and S. W. Lee, Insight into phosphate doped $BiVO_4$ heterostructure for multifunctional photocatalytic performances: A combined experimental and DFT study, *Appl. Surf. Sci.*, 2019, **466**, 787–800.

18 J. Fardush Tanha, S. Farhad, U. Honey, N. Tanvir, T. Hasan and S. Shahriyar Nishat, *et al.*, A DFT+U look into experimentally synthesized monoclinic scheelite $BiVO_4$, *J. Appl. Phys.*, 2021, **130**(23), 235107.

19 M. L. Guan, D. K. Ma, S. W. Hu, Y. J. Chen and S. M. Huang, From hollow olive-shaped $BiVO_4$ to n- p core-shell $BiVO_4$ @ Bi_2O_3 microspheres: Controlled synthesis and enhanced visible-light-responsive photocatalytic properties, *Inorg. Chem.*, 2011, **50**(3), 800–805.

20 F. F. Abdi and S. P. Berglund, Recent developments in complex metal oxide photoelectrodes, *J. Phys. D: Appl. Phys.*, 2017, **50**(19), 193002.

21 F. F. Abdi and R. van de Krol, Nature and light dependence of bulk recombination in Co-Pi-catalyzed $BiVO_4$ photoanodes, *J. Phys. Chem. C*, 2012, **116**(17), 9398–9404.

22 G. V. Govindaraju, J. M. Morbec, G. A. Galli and K. S. Choi, Experimental and computational investigation of lanthanide ion doping on $BiVO_4$ photoanodes for solar water splitting, *J. Phys. Chem. C*, 2018, **122**(34), 19416–19424.

23 T. He, Y. Zhao, D. Benetti, B. Moss, L. Tian and S. Selim, *et al.*, Facet-engineered $BiVO_4$ photocatalysts for water oxidation: lifetime gain versus energetic loss, *J. Am. Chem. Soc.*, 2024, **146**(39), 27080–27089.

24 H. S. Han, S. Shin, D. H. Kim, I. J. Park, J. S. Kim and P. S. Huang, *et al.*, Boosting the solar water oxidation performance of a $BiVO_4$ photoanode by crystallographic orientation control, *Energy Environ. Sci.*, 2018, **11**(5), 1299–1306.

25 C. Hu, M. Tian, L. Wu and L. Chen, Enhanced photocatalytic degradation of paraben preservative over designed g-C_3N_4/$BiVO_4$ S-scheme system and toxicity assessment, *Ecotoxicol. Environ. Saf.*, 2022, **231**, 113175.

26 L. Xia, J. Bai, J. Li, Q. Zeng, L. Li and B. Zhou, High-performance $BiVO_4$ photoanodes cocatalyzed with an ultrathin α -Fe_2O_3 layer for photoelectrochemical application, *Appl. Catal., B*, 2017, **204**, 127–133.

27 H. L. Tan, R. Amal and Y. H. Ng, Alternative strategies in improving the photocatalytic and photoelectrochemical activities of visible light-driven $BiVO_4$: A review, *J. Mater. Chem. A*, 2017, **5**(32), 16498–16521.

28 J. H. Kim and J. S. Lee, Elaborately modified $BiVO_4$ photoanodes for solar water splitting, *Adv. Mater.*, 2019, **31**(20), 1806938.

29 M. Noor, F. Sharmin, M. Al Mamun, S. Hasan, M. Hakim and M. Basith, Effect of Gd and Y co-doping in $BiVO_4$

photocatalyst for enhanced degradation of methylene blue dye, *J. Alloys Compd.*, 2022, **895**, 162639.

30 S. Obregón and G. Colón, Improved O_2 evolution from a water splitting reaction over Er^{3+} and Y^{3+} co-doped tetragonal $BiVO_4$, *Catal. Sci. Technol.*, 2014, **4**(7), 2042–2050.

31 J. Jia, M. Zhang, Z. Liu, C. Yu, W. Zhou and Z. Li, La^{3+}, Gd^{3+} -codoped $BiVO_4$ nanorods with superior visible-light-driven photocatalytic performance for simultaneous removing aqueous Cr (VI) and azo dye, *J. Nanopart. Res.*, 2020, **22**(9), 275.

32 N. Singh, U. Kumar, N. Jatav and I. Sinha, Photocatalytic degradation of crystal violet on Cu, Zn doped $BiVO_4$ particles, *Langmuir*, 2024, **40**(16), 8450–8462.

33 F. K. Naqvi, S. Beg and K. Anwar, Synthesis of visible light active copper, iron co-doped $BiVO_4$ photocatalyst for the degradation of phenol, *React. Kinet., Mech. Catal.*, 2020, **131**(1), 409–422.

34 N. Singh and I. Sinha, Development of Cu, Mn Codoped $BiVO_4$ ($Cu_xMn_{0.03-x}Bi_{1-x}V_{0.97+x}O_4$) Photocatalyst for Photo-Fenton Degradation of Ciprofloxacin, *Langmuir*, 2025, **41**(23), 14935–14945.

35 T. A. Mahi, Q. S. Hossain, S. S. Nishat, S. Ahmed, M. Khan and M. S. Bashar, *et al.*, A Combined Experimental and First Principles Look into (Ce, Mo) Doped $BiVO_4$, *Heliyon*, 2024, **10**(8), e29408.

36 M. M. Sajid, H. Zhai, M. A. Iqbal, N. A. Shad and A. M. Munawar, Tunable Fe^{+3} and W^{+6} Co-doped $BiVO_4$ nanohybrids with efficient photocatalytic and electrochemical chemical sensing characteristics, *Ceram. Int.*, 2024, **50**(1), 957–968.

37 S. Saxena, A. Verma, N. K. Biswas, S. A. Khan, V. R. Satsangi and R. Shrivastav, *et al.*, Zr-W Co-doping in $BiVO_4$ -Synergistic effect in photoelectrochemical water splitting, *Mater. Chem. Phys.*, 2021, **267**, 124675.

38 S. Sriwichai, R. Irani, F. Xi, D. Friedrich, C. Höhn and I. Y. Ahmet, *et al.*, Role of Gd in Enhancing the Charge Carrier Mobility of Spray-Deposited $BiVO_4$ Photoanodes, *Solar RRL*, 2021, **5**(8), 2100268.

39 S. Bashir, A. Jamil, M. S. Khan, A. Alazmi, F. A. Abuilaiwi and M. Shahid, Gd-doped $BiVO_4$ microstructure and its composite with a flat carbonaceous matrix to boost photocatalytic performance, *J. Alloys Compd.*, 2022, **913**, 165214.

40 K. Ding, B. Chen, Z. Fang, Y. Zhang and Z. Chen, Why the photocatalytic activity of Mo-doped $BiVO_4$ is enhanced: A comprehensive density functional study, *Phys. Chem. Chem. Phys.*, 2014, **16**(26), 13465–13476.

41 Y. Park, D. Kang and K. S. Choi, Marked enhancement in electron-hole separation achieved in the low bias region using electrochemically prepared Mo-doped $BiVO_4$ photoanodes, *Phys. Chem. Chem. Phys.*, 2014, **16**(3), 1238–1246.

42 S. M. Thalluri, S. Hernandez, S. Bensaid, G. Saracco and N. Russo, Green-synthesized W-and Mo-doped $BiVO_4$ oriented along the {0 4 0} facet with enhanced activity for the sun-driven water oxidation, *Appl. Catal., B*, 2016, **180**, 630–636.

43 M. Rohloff, B. Anke, S. Zhang, U. Gernert, C. Scheu and M. Lerch, *et al.*, Mo-doped $BiVO_4$ thin films-high photoelectrochemical water splitting performance achieved by a tailored structure and morphology. Sustain, *Energy Fuels*, 2017, **1**(8), 1830–1846.

44 M. Tayebi, A. Tayyebi and B. K. Lee, Improved photoelectrochemical performance of molybdenum (Mo)-doped monoclinic bismuth vanadate with increasing donor concentration, *Catal. Today*, 2019, **328**, 35–42.

45 C. Liu, H. Luo, Y. Xu, Z. Zhang, Q. Liang and W. Wang, *et al.*, Synergistic cocatalytic effect of ultra-thin metal-organic framework and Mo-dopant for efficient photoelectrochemical water oxidation on $BiVO_4$ photoanode, *Chem. Eng. J.*, 2020, **384**, 123333.

46 G. Kresse and J. Furthmüller, Efficient iterative schemes for ab initio total-energy calculations using a plane-wave basis set, *Phys. Rev. B: Condens. Matter Mater. Phys.*, 1996, **54**(16), 11169.

47 G. Kresse and D. Joubert, From ultrasoft pseudopotentials to the projector augmented-wave method, *Phys. Rev. B: Condens. Matter Mater. Phys.*, 1999, **59**(3), 1758.

48 P. E. Blöchl, Projector augmented-wave method, *Phys. Rev. B: Condens. Matter Mater. Phys.*, 1994, **50**(24), 17953.

49 A. Jain, Y. Shin and K. A. Persson, Computational predictions of energy materials using density functional theory, *Nat. Rev. Mater.*, 2016, **1**(1), 1–13.

50 R. O. Jones, Density functional theory: Its origins, rise to prominence, and future, *Rev. Mod. Phys.*, 2015, **87**(3), 897.

51 M. Z. Hossain, S. S. Nishat, S. Ahmed, Q. S. Hossain, M. N. I. Khan and T. Hasan, *et al.*, Combined experimental and DFT approach to $BiNbO_4$ polymorphs, *RSC Adv.*, 2023, **13**(8), 5576–5589.

52 Q. S. Hossain, S. Ahmed, S. S. Nishat, M. Z. Hossain, M. N. I. Khan and T. Hasan, *et al.*, An ab initio DFT perspective on experimentally synthesized $CuBi_2O_4$, *RSC Adv.*, 2023, **13**(21), 14291–14305.

53 S. Ahmed, S. S. Nishat, A. Kabir, A. S. H. Faysal, T. Hasan and S. Chakraborty, *et al.*, Structural, elastic, vibrational, electronic and optical properties of $SmFeO_3$ using density functional theory, *Phys. B: Condens. Mater.*, 2021, **615**, 413061.

54 S. Ahmed, T. Hasan, A. S. H. Faysal, S. S. Nishat, M. N. I. Khan and A. Kabir, *et al.*, A DFT+U approach to doped $SrTiO_3$ for solar harvesting applications, *Comput. Mater. Sci.*, 2022, **214**, 111743.

55 Q. S. Hossain, S. S. Nishat, M. Sultana, T. A. Mahi, S. Ahmed and M. N. I. Khan, *et al.*, A combined first principles and experimental approach to Bi_2WO_6, *RSC Adv.*, 2023, **13**(51), 36130–36143.

56 S. Saroar, S. Sultana, Q. S. Hossain, S. S. Nishat, I. H. Sabuj and S. A. Jahan, *et al.*, Ab Initio DFT Perspective on Triclinic Bi_2CrO_6: Energy Material for Optoelectronic, Thermoelectric, and Photocatalytic Applications, *J. Phys. Chem. C*, 2025, **129**(25), 11732–11745.

57 K. Tao, J. Zhou, Q. Sun, Q. Wang, V. Stepanyuk and P. Jena, Self-consistent determination of Hubbard U for explaining the anomalous magnetism of the Gd13 cluster, *Phys. Rev. B: Condens. Matter Mater. Phys.*, 2014, **89**(8), 085103.

58 J. H. Baek, T. M. Gill, H. Abroshan, S. Park, X. Shi and J. Nørskov, et al., Selective and efficient Gd-doped BiVO$_4$ photoanode for two-electron water oxidation to H$_2$O$_2$, ACS Energy Lett., 2019, 4(3), 720–728.

59 J. Yu and A. Kudo, Effects of structural variation on the photocatalytic performance of hydrothermally synthesized BiVO$_4$, Adv. Func. Mater., 2006, 16(16), 2163–2169.

60 H. Xu, C. Wu, H. Li, J. Chu, G. Sun and Y. Xu, et al., Synthesis, characterization and photocatalytic activities of rare earth-loaded BiVO$_4$ catalysts, Appl. Surf. Sci., 2009, 256(3), 597–602.

61 S. Usai, S. Obregón, A. I. Becerro and G. Colón, Monoclinic-tetragonal heterostructured BiVO$_4$ by yttrium doping with improved photocatalytic activity, J. Phys. Chem. C, 2013, 117(46), 24479–24484.

62 Y. Guo, X. Yang, F. Ma, K. Li, L. Xu and X. Yuan, et al., Additive-free controllable fabrication of bismuth vanadates and their photocatalytic activity toward dye degradation, Appl. Surf. Sci., 2010, 256(7), 2215–2222.

63 A. Bhattacharya, K. Mallick and A. Hartridge, Phase transition in BiVO$_4$, Mater. Lett., 1997, 30(1), 7–13.

64 I. Abdellaoui, M. M. Islam, M. Remeika, Y. Higuchi, T. Kawaguchi and T. Harada, et al., Photocarrier recombination dynamics in BiVO$_4$ for visible light-driven water oxidation, J. Phys. Chem. C, 2020, 124(7), 3962–3972.

65 X. Li, L. Xu, X. Li, M. Hu, R. Huang and C. Huang, Oxidant peroxo-synthesized monoclinic BiVO$_4$: Insights into the crystal structure deformation and the thermochromic properties, J. Alloys Compd., 2019, 787, 666–671.

66 Y. Lin, C. Lu and C. Wei, Microstructure and photocatalytic performance of BiVO$_4$ prepared by hydrothermal method, J. Alloys Compd., 2019, 781, 56–63.

67 J. Pellicer-Porres, D. Vazquez-Socorro, S. López-Moreno, A. Muñoz, P. Rodrguez-Hernández and D. Martnez-Garca, et al., Phase transition systematics in BiVO$_4$ by means of high-pressure-high-temperature Raman experiments, Phys. Rev. B, 2018, 98(21), 214109.

68 R. L. Frost, D. A. Henry, M. L. Weier and W. Martens, Raman spectroscopy of three polymorphs of BiVO$_4$: clinobisvanite, dreyerite and pucherite, with comparisons to -bearing minerals: namibite, pottsite and schumacherite, J. Raman Spectrosc., 2006, 37(7), 722–732.

69 T. S. Dabodiya, P. Selvarasu and A. V. Murugan, Tetragonal to monoclinic crystalline phases change of BiVO$_4$ via microwave-hydrothermal reaction: In correlation with visible-light-driven photocatalytic performance, Inorg. Chem., 2019, 58(8), 5096–5110.

70 F. D. Hardcastle and I. E. Wachs, Determination of vanadium-oxygen bond distances and bond orders by Raman spectroscopy, J. Phys. Chem., 1991, 95(13), 5031–5041.

71 V. T. Pham, B. T. T. Dao, H. T. T. Nguyen, N. Q. Tran, D. T. L. Hang and N. D. Trung, et al., Substitution of V^{5+} in BiVO$_4$ with Ni^{2+} and the improved photocatalytic degradation of crystal violet under white LED light irradiation, Top. Catal., 2023, 66(1), 2–11.

72 U. G. Pérez, S. Sepúlveda-Guzmán, A. Martnez-De La Cruz and U. O. Méndez, Photocatalytic activity of BiVO$_4$ nanospheres obtained by solution combustion synthesis using sodium carboxymethylcellulose, J. Mol. Catal. A: Chem., 2011, 335(1–2), 169–175.

73 M. Gotic, S. Music, M. Ivanda, M. Šoufek and S. Popovic, Synthesis and characterisation of bismuth (III) vanadate, J. Mol. Struct., 2005, 744, 535–540.

74 K. Hirota, G. Komatsu, M. Yamashita, H. Takemura and O. Yamaguchi, Formation, characterization and sintering of alkoxy-derived bismuth vanadate, Mater. Res. Bull., 1992, 27(7), 823–830.

75 D. Ke, T. Peng, L. Ma, P. Cai and K. Dai, Effects of hydrothermal temperature on the microstructures of BiVO$_4$ and its photocatalytic O$_2$ evolution activity under visible light, Inorg. Chem., 2009, 48(11), 4685–4691.

76 A. Zhang and J. Zhang, The effect of hydrothermal temperature on the synthesis of monoclinic bismuth vanadate powders, Materials Science-Poland, 2009, vol. 27, no. 4/1.

77 J. Liu, H. Wang, S. Wang and H. Yan, Hydrothermal preparation of BiVO$_4$ powders, Mater. Sci. Eng. B, 2003, 104(1–2), 36–39.

78 S. Li, Y. Cheng, Q. Wang, C. Liu and L. Xu, Design, fabrication and characterization of photocatalyst Ni-doped BiVO$_4$ for high effectively degrading dye contaminant, Mater. Res. Express, 2020, 7(11), 115005.

79 D. P. Jaihindh, B. Thirumalraj, S. M. Chen, P. Balasubramanian and Y. P. Fu, Facile synthesis of hierarchically nanostructured bismuth vanadate: an efficient photocatalyst for degradation and detection of hexavalent chromium, J. Hazard. Mater., 2019, 367, 647–657.

80 S. Gu, W. Li, F. Wang, S. Wang, H. Zhou and H. Li, Synthesis of buckhorn-like BiVO$_4$ with a shell of CeO$_x$ nanodots: Effect of heterojunction structure on the enhancement of photocatalytic activity, Appl. Catal., B, 2015, 170, 186–194.

81 Z. Jiang, Y. Liu, T. Jing, B. Huang, X. Zhang and X. Qin, et al., Enhancing the photocatalytic activity of BiVO$_4$ for oxygen evolution by Ce doping: Ce^{3+} ions as hole traps, J. Phys. Chem. C, 2016, 120(4), 2058–2063.

82 Y. Luo, G. Tan, G. Dong, H. Ren and A. Xia, Effects of structure, morphology, and up-conversion on Nd-doped BiVO$_4$ system with high photocatalytic activity, Ceram. Int., 2015, 41(2), 3259–3268.

83 M. Du Plessis, Relationship between specific surface area and pore dimension of high porosity nanoporous silicon-Model and experiment, Phys. Status Solidi, 2007, 204(7), 2319–2328.

84 P. Pookmanee, S. Kojinok, R. Puntharod, S. Sangsrichan and S. Phanichphant, Preparation and characterization of BiVO$_4$ powder by the sol-gel method, Ferroelectrics, 2013, 456(1), 45–54.

85 N. M. Maalej, A. Qurashi, A. A. Assadi, R. Maalej, M. N. Shaikh and M. Ilyas, et al., Synthesis of Gd$_2$O$_3$: Eu nanoplatelets for MRI and fluorescence imaging, Nanoscale Res. Lett., 2015, 10, 1–10.

86 Y. Li, Z. Liu, W. Qi, H. Shi, K. Wang and X. Wang, *et al.*, Bifunctional reality of Gd doping to boost the photocatalytic H_2O_2 production of Au/$BiVO_4$, *Appl. Surf. Sci.*, 2024, **656**, 159664.

87 V. I. Merupo, S. Velumani, K. Ordon, N. Errien, J. Szade and A. H. Kassiba, Structural and optical characterization of ball-milled copper-doped bismuth vanadium oxide ($BiVO_4$), *CrystEngComm*, 2015, **17**(17), 3366–3375.

88 M. Beetz, S. Häringer, P. Elsässer, J. Kampmann, L. Sauerland and F. Wolf, *et al.*, Ultra-Thin Protective Coatings for Sustained Photoelectrochemical Water Oxidation with Mo: $BiVO_4$, *Adv. Funct. Mater.*, 2021, **31**(45), 2011210.

89 S. S. Mali, G. R. Park, H. Kim, H. H. Kim, J. V. Patil and C. K. Hong, Synthesis of nanoporous Mo:$BiVO_4$ thin film photoanodes using the ultrasonic spray technique for visible-light water splitting, *Nanoscale Adv.*, 2019, **1**(2), 799–806.

90 J. Jian, Y. Xu, X. Yang, W. Liu, M. Fu and H. Yu, *et al.*, Embedding laser generated nanocrystals in $BiVO_4$ photoanode for efficient photoelectrochemical water splitting, *Nat. Commun.*, 2019, **10**(1), 2609.

91 S. Ahmed, A. S. H. Faysal, M. N. I. Khan, M. Basith, M. S. Bashar and H. Das, *et al.*, Room temperature ferroic orders in Zr and (Zr, Ni) doped $SrTiO_3$, *Results Phys.*, 2021, **31**, 104940.

92 M. Valant, T. Kolodiazhnyi, I. Arcon, F. Aguesse, A. K. Axelsson and N. M. Alford, The Origin of Magnetism in Mn-Doped $SrTiO_3$, *Adv. Funct. Mater.*, 2012, **22**(10), 2114–2122.

93 A. P. Singh, N. Kodan, A. Dey, S. Krishnamurthy and B. R. Mehta, Improvement in the structural, optical, electronic and photoelectrochemical properties of hydrogen treated bismuth vanadate thin films, *Int. J. Hydrogen*, 2015, **40**(12), 4311–4319.

94 T. A. Mahi, I. H. Sabuj, Q. S. Hossain, S. S. Nishat, S. A. Jahan and M. N. I. Khan, *et al.*, First-Principles Modeling of Lattice Dynamics and Direct Electronic Transition in Halide Double Perovskite $Cs_2NaBiCl_6$, *J. Phys. Chem. C*, 2024, **128**, 20468–20480.

95 S. Saroar, S. Sultana, S. S. Nishat, Q. S. Hossain, M. Khan and D. Islam, *et al.*, First-Principles Calculations on Electronic, Optical, and Phonon Properties of γ-Bi_2MoO_6, *ACS Omega*, 2024, **9**(34), 36314–36325.

96 L. Chen, E. Alarcón-Lladó, M. Hettick, I. D. Sharp, Y. Lin and A. Javey, *et al.*, Reactive sputtering of bismuth vanadate photoanodes for solar water splitting, *J. Phys. Chem. C*, 2013, **117**(42), 21635–21642.

97 S. Wang, T. He, P. Chen, A. Du, K. Ostrikov and W. Huang, *et al.*, In situ formation of oxygen vacancies achieving near-complete charge separation in planar $BiVO_4$ photoanodes, *Adv. Mater.*, 2020, **32**(26), 2001385.

98 D. Raiser and J. Deville, Study of XPS photoemission of some gadolinium compounds, *J. Electron Spectrosc. Relat. Phenom.*, 1991, **57**(1), 91–97.

99 W. Luo, J. Wang, X. Zhao, Z. Zhao, Z. Li and Z. Zou, Formation energy and photoelectrochemical properties of $BiVO_4$ after doping at Bi^{3+} or V^{5+} sites with higher valence metal ions, *Phys. Chem. Chem. Phys.*, 2013, **15**(3), 1006–1013.

100 L. Wang, X. Gu, Y. Zhao, M. Wei, Y. Qiang and Y. Zhao, Enhanced photoelectrochemical performance by doping Mo into $BiVO_4$ lattice, *J. Mater. Sci.: Mater. Electron.*, 2018, **29**, 19278–19286.

101 T. W. Kim, Y. Ping, G. A. Galli and K. S. Choi, Simultaneous enhancements in photon absorption and charge transport of bismuth vanadate photoanodes for solar water splitting, *Nat. Commun.*, 2015, **6**(1), 8769.

102 K. P. S. Parmar, H. J. Kang, A. Bist, P. Dua, J. S. Jang and J. S. Lee, Photocatalytic and photoelectrochemical water oxidation over metal-doped monoclinic $BiVO_4$ photoanodes, *ChemSusChem*, 2012, **5**(10), 1926–1934.

103 A. Podborska, B. Gawel, Ł. Pietrzak, I. B. Szymanska, J. K. Jeszka and W. Asocha, *et al.*, Anomalous photocathodic behavior of CdS within the Urbach tail region, *J. Phys. Chem. C*, 2009, **113**(16), 6774–6784.

104 P. Kwolek, K. Pilarczyk, T. Tokarski, K. Lewandowska and K. Szacilowski, $Bi_xLa_{(1−x)}VO_4$ solid solutions: tuning of electronic properties via stoichiometry modifications, *Nanoscale*, 2014, **6**(4), 2244–2254.

105 H. S. Park, K. E. Kweon, H. Ye, E. Paek, G. S. Hwang and A. J. Bard, Factors in the metal doping of $BiVO_4$ for improved photoelectrocatalytic activity as studied by scanning electrochemical microscopy and first-principles density-functional calculation, *J. Phys. Chem. C*, 2011, **115**(36), 17870–17879.

106 J. Zhang, M. Deng, F. Ren, Y. Wu and Y. Wang, Effects of Mo/W codoping on the visible-light photocatalytic activity of monoclinic $BiVO_4$ within the GGA + U framework, *RSC Adv.*, 2016, **6**(15), 12290–12297.

107 J. C. Yu, J. Yu, W. Ho and Z. Jiang, Effects of F-doping on the photocatalytic activity and microstructures of nanocrystalline TiO_2 powders, *Chem. Mater.*, 2002, **14**(9), 3808–3816.

108 R. Georgekutty, M. K. Seery and S. C. Pillai, A highly efficient Ag-ZnO photocatalyst: synthesis, properties, and mechanism, *J. Phys. Chem. C*, 2008, **112**(35), 13563–13570.

109 Q. C. Xu, D. V. Wellia, Y. H. Ng, R. Amal and T. T. Y. Tan, Synthesis of porous and visible-light absorbing Bi_2WO_6/TiO_2 heterojunction films with improved photoelectrochemical and photocatalytic performances, *J. Phys. Chem. C*, 2011, **115**(15), 7419–7428.

110 L. Chen, S. F. Yin, R. Huang, Q. Zhang, S. L. Luo and C. T. Au, Hollow peanut-like m-$BiVO_4$: facile synthesis and solar-light-induced photocatalytic property, *CrystEngComm*, 2012, **14**(12), 4217–4222.

111 H. Cheng, B. Huang, Y. Dai, X. Qin and X. Zhang, One-step synthesis of the nanostructured AgI/BiOI composites with highly enhanced visible-light photocatalytic performances, *Langmuir*, 2010, **26**(9), 6618–6624.

112 C. Yu, K. Yang, C. Y. Jimmy, F. Cao, X. Li and X. Zhou, Fast fabrication of Co_3O_4 and CuO/$BiVO_4$ composite photocatalysts with high crystallinity and enhanced photocatalytic

activity via ultrasound irradiation, *J. Alloys Compd.*, 2011, **509**(13), 4547–4552.

113 L. Chen, Q. Zhang, R. Huang, S. F. Yin, S. L. Luo and C. T. Au, Porous peanut-like Bi_2O_3-$BiVO_4$ composites with heterojunctions: one-step synthesis and their photocatalytic properties, *Dalton Trans.*, 2012, **41**(31), 9513–9518.

114 X. Zhu, F. Zhang, M. Wang, X. Gao, Y. Luo and J. Xue, *et al.*, A shuriken-shaped m-$BiVO_4$/001-TiO_2 heterojunction: synthesis, structure and enhanced visible light photocatalytic activity, *Appl. Catal., A*, 2016, **521**, 42–49.

115 C. Yu, S. Dong, J. Zhao, X. Han, J. Wang and J. Sun, Preparation and characterization of sphere-shaped $BiVO_4$/reduced graphene oxide photocatalyst for an augmented natural sunlight photocatalytic activity, *J. Alloys Compd.*, 2016, **677**, 219–227.

116 I. H. Sabuj, S. A. Jahan, M. N. I. Khan, U. S. Akhtar, D. Islam and M. S. Bashar, *et al.*, An experimental Look into efficient quaternary Bi_5O_7 I/$Bi(IO_3)_3$/Bi_2 $(IO_4)(IO_3)_3$/$BiOIO_3$ Photocatalytic Composite, *AIP Adv.*, 2024, **14**, 035146.

117 M. R. Haq, N. Ehsan, S. S. Nishat, Q. S. Hossain, M. N. I. Khan and M. Shahriar Bashar, *et al.*, Comprehensive First-Principles Modeling of Experimentally Synthesized $BiPO_4$ Polymorphs, *J. Phys. Chem. C*, 2024, **128**(11), 4779–4788.

118 M. Muradov, S. Mammadyarova, G. Eyvazova, O. Balayeva, I. Hasanova and G. Aliyeva, *et al.*, The effect of Cu doping on structural, optical properties and photocatalytic activity of Co_3O_4 nanoparticles synthesized by sonochemical method, *Opt. Mater.*, 2023, **142**, 114001.

119 M. Muradov, S. Mammadyarova, G. Eyvazova, O. Balayeva, G. Aliyeva and I. Hasanova, *et al.*, Synthesis of $Cu_xCo_{3-x}O_4$ nanoparticles by a sonochemical method and characterization of structural and optical properties and photocatalytic activity for the degradation of methylene blue, *RSC Adv.*, 2024, **14**(2), 1082–1093.

120 Y. Luo, G. Tan, G. Dong, H. Ren and A. Xia, A comprehensive investigation of tetragonal Gd-doped $BiVO_4$ with enhanced photocatalytic performance under sun-light, *Appl. Surf. Sci.*, 2016, **364**, 156–165.

121 B. Zhang, S. Yu, Y. Dai, X. Huang, L. Chou and G. Lu, *et al.*, Nitrogen-incorporation activates $NiFeO_x$ catalysts for efficiently boosting oxygen evolution activity and stability of $BiVO_4$ photoanodes, *Nat. Commun.*, 2021, **12**(1), 6969.

122 P. Newhouse, D. Guevarra, M. Umehara, S. Reyes-Lillo, L. Zhou and D. Boyd, *et al.*, Combinatorial alloying improves bismuth vanadate photoanodes via reduced monoclinic distortion, *Energy Environ. Sci.*, 2018, **11**(9), 2444–2457.